

Measurement and prediction of bottom boundary layer hydrodynamics under modulated oscillatory flows

O'Donoghue, T.; Davies, A.G.; Bhawanin, M.; Van Der A, D.A.

Coastal Engineering

DOI:

[10.1016/j.coastaleng.2021.103954](https://doi.org/10.1016/j.coastaleng.2021.103954)

Published: 01/10/2021

Peer reviewed version

[Cyswllt i'r cyhoeddiad / Link to publication](#)

Dyfyniad o'r fersiwn a gyhoeddwyd / Citation for published version (APA):

O'Donoghue, T., Davies, A. G., Bhawanin, M., & Van Der A, D. A. (2021). Measurement and prediction of bottom boundary layer hydrodynamics under modulated oscillatory flows. *Coastal Engineering*, 169(103954), Article 103954. <https://doi.org/10.1016/j.coastaleng.2021.103954>

Hawliau Cyffredinol / General rights

Copyright and moral rights for the publications made accessible in the public portal are retained by the authors and/or other copyright owners and it is a condition of accessing publications that users recognise and abide by the legal requirements associated with these rights.

- Users may download and print one copy of any publication from the public portal for the purpose of private study or research.
- You may not further distribute the material or use it for any profit-making activity or commercial gain
- You may freely distribute the URL identifying the publication in the public portal ?

Take down policy

If you believe that this document breaches copyright please contact us providing details, and we will remove access to the work immediately and investigate your claim.

Measurement and prediction of bottom boundary layer hydrodynamics under modulated oscillatory flows

T. O'Donoghue^{a,*}, A.G. Davies^b, M. Bhawanin^c, D.A. van der A^a

^a*School of Engineering, University of Aberdeen, UK*

^b*School of Ocean Sciences, Bangor University, UK*

^c*Tensar International Corp., Malaysia (Former PhD student, University of Aberdeen)*

Abstract

Velocities are measured using LDA within the bottom boundary layer for 10 oscillatory flow tunnel experiments involving regular and amplitude modulated oscillatory flows over a gravel-rough bed and a sand-rough bed. Corresponding regular and modulated flows were equivalent in terms of rms velocity, oscillatory flow period, skewness and asymmetry. The experimental results are compared with predictions based on a 1DV RANS model with $k - \epsilon$ turbulence closure. The effects of modulation on the hydrodynamics of individual flow half-cycles and on the time-averaged hydrodynamics are analysed. Turbulence is carried over from one half-cycle to the following half-cycle but the main hydrodynamic properties within a half-cycle (boundary layer thickness, peak turbulent kinetic energy, peak turbulent stress) show little or no dependence on prior half-cycle flow conditions. Turbulence propagation from the bed and vertical profiles of skewness, asymmetry, time-averaged turbulent kinetic energy and time-averaged turbulent stress show remarkably little effect of modulation. Modulation does not affect the shape of the time-averaged velocity profile generated by the non-symmetric flows, but it does reduce the magnitude. The RANS model shows generally good agreement with the measured hydrodynamics above about one grain diameter from the bed, but, because of its assumption of rough turbulent flow, poorly predicts the hydrodynamics of the low-velocity half-cycles of the

*Corresponding author

Email address: `t.odonoghue@abdn.ac.uk` (T. O'Donoghue)

modulated flows over the sand-rough bed.

Keywords: oscillatory flow, modulated flow, boundary layer, turbulence, flow tunnel, RANS model

1. Introduction

Understanding and predicting how the seabed responds to waves requires knowledge of the hydrodynamics within the wave bottom boundary layer. Present knowledge is largely based on experiments conducted in flow tunnels, in which
5 oscillatory flows are generated over fixed beds of different roughness, and velocities are measured at elevations extending from the bed to the free-stream. In such experiments, the hydraulic conditions are defined by the flow Reynolds number, $Re = ua/\nu$, and the bed relative roughness, a/k_s , (u is horizontal velocity amplitude, a is horizontal water particle displacement amplitude, ν is
10 the water kinematic viscosity and k_s is the bed roughness). In large tunnels, field-scale hydraulic conditions can be realised with Re reaching 10^7 . The most notable large-scale oscillatory flow tunnel studies include the sinusoidal flow experiments of Jonsson (1963), Jonsson & Carlsen (1976), Sleath (1987) and Jensen et al. (1989) and, more recently, the velocity-asymmetric and velocity-
15 skewed experiments of van der A et al. (2011) and Yuan & Madsen (2014) involving various bed roughness. For the latter two studies, the velocities were measured using PIV and results were obtained for turbulent kinetic energy and turbulent stress. van der A et al. (2018) used LDA to measure higher-order turbulence statistics for velocity-asymmetric flows over a smooth bed and obtained
20 good agreement with corresponding results from DNS.

The combined previous research has yielded comprehensive knowledge of phase- and time-averaged velocities and turbulence through the oscillatory bottom boundary layer for regular flows. However, real sea wave conditions are irregular, which means the bottom boundary layer hydrodynamics vary wave
25 to wave, giving rise to the possibility of history effects, by which the hydrodynamics under an individual wave may be influenced by the hydrodynamics of

the preceeding wave(s). In addition, the irregularity may influence the time-averaged flow such that the time-averaged hydrodynamics under “equivalent” regular and irregular waves are not the same.

30 History effects in irregular oscillatory flows were studied in experiments reported by Yuan & Dash (2017) in which two types of irregular flow were generated in a flow tunnel. The first type was produced by amplitude modulating skewed or asymmetric regular flows. The second type was produced by randomly re-sequencing the individual flow cycles from the modulated flow group;
 35 the modulated sequence and the random sequence therefore contained the same flow cycles but in different order. To examine the effects of irregularity, Yuan & Dash (2017) compared the measured hydrodynamics of selected corresponding flow cycles from the two sequences. Their main conclusion was that history effects are noticeable at the early stage of a new flow cycle and are stronger when
 40 the preceding flow cycle has large amplitude. Turbulence from the preceding flow cycle dominates the boundary layer at this early stage, but becomes subsumed by the developing turbulence of the new flow cycle as the flow accelerates, and ultimately has little influence on the main boundary layer properties of the new cycle.

45 The present paper reports on experiments that complement Yuan & Dash (2017). The experiments were conducted in a large oscillatory flow tunnel and involved “equivalent” regular and modulated oscillatory flows over two beds of different roughness, where equivalence here means corresponding regular and modulated flows having the same flow-cycle period, root-mean-square velocity,
 50 velocity skewness and velocity asymmetry. The range of regular and modulated flow conditions enables assessment of history effects on the hydrodynamics of individual flow cycles, similar to Yuan & Dash (2017). In addition, the equivalence in terms of period, root-mean-square velocity, skewness and asymmetry enables isolation and measurement of the effects of velocity amplitude variability
 55 on the time-averaged boundary layer hydrodynamics.

Many previous studies have shown the ability of two-equation 1DV RANS models, with various refinements, to predict reasonably well the intra-period

and time-averaged boundary layer hydrodynamics for regular oscillatory flows (e.g. Justesen, 1991; Sana & Tanaka, 2000; Foti & Scandura, 2004; Sana et al., 2009; Cavallaro et al., 2011). Holmedal et al. (2003) used a 1DV model to study the rough turbulent bottom boundary layer under random waves, with and without a superimposed mean current. They present results for the predicted velocity and turbulence structure within the bottom boundary layer, but without comparison to experimental data. In the present paper we apply a high-Re 1DV RANS model with $k - \epsilon$ turbulence closure, similar to that of Holmedal et al. (2003), to the experimental conditions and compare model predictions to measurements of time-varying and time-averaged velocities, turbulent kinetic energy and turbulent stress. To the authors' knowledge, this is the first time that this type of model has been tested against detailed measurements for full-scale non-regular oscillatory flow conditions.

The experimental set-up, test conditions and measurements, including determination of the bed roughness for the two bed types, are described in Section 2. The numerical model and its application to the experimental cases are outlined in Section 3. The experimental and model results for boundary layer velocities, turbulent kinetic energy and turbulent stress are presented and compared in Section 4. The main conclusions are presented in Section 5.

2. Experimental set-up and test conditions

2.1. Experimental facility

The experiments were conducted in the Aberdeen Oscillatory Flow Tunnel (AOFT). The facility has a U-tube configuration, with an overall length of 16 m, 10 m of which comprises a glass-sided rectangular test section that is 0.75 m high and 0.3 m wide. The present experiments follow a similar set-up to that described by van der A et al. (2011), having a 7 m-long, 0.25 m-high false floor built into the test section with 1:4 ramps at each end connecting the false bed to the tunnel floor. Horizontally-uniform oscillatory flows are generated by an electro-hydraulically-controlled 1 m-diameter piston located at one end of the

tunnel. With the false floor in place, oscillatory flows with water displacement amplitude up to 1.5 m can be generated in the test section.

2.2. Experimental conditions

90 The experiments involved velocity measurements over two fixed beds of different roughness: a sand-rough bed comprising well-sorted sand with $d_{50} = 0.46$ mm and a gravel-rough bed comprising 5.65 mm (d_{50}) gravel. For the sand-rough bed, a thin sheet of adhesive-backed plastic was first bonded to the PVC panels of the false floor; the plastic was then coated with marine varnish and
 95 the sand sprinkled on top. On completion of the sand-rough experiments, the sediment was removed by peeling the sediment-laden plastic off the PVC panels and the panels were then used for the gravel-rough experiments. For the gravel-rough bed, a 2 mm-thick stainless steel sheet was fixed to the PVC panels and the gravel was bonded to the sheets using marine varnish. [Figure 1 shows the](#)
 100 [two beds.](#)

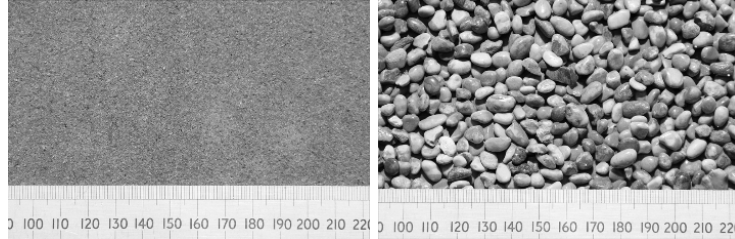


Figure 1: Photograph of (left) the sand-rough bed and (right) the gravel-rough bed; the numbers on the scales are mm.

Ten experiments in total were carried out, comprising 8 oscillatory flows over the sand-rough bed and 2 oscillatory flows over the gravel-rough bed (Table 1). The regular flows were sinusoidal, skewed or asymmetric, synthesised using (Abreu et al., 2010)

$$u_r(t) = U \sqrt{1 - r^2} \left(\frac{\sin(\omega t) + \frac{r \sin \phi}{1 + \sqrt{1 - r^2}}}{1 - r \cos(\omega t + \phi)} \right) \quad (1)$$

105

where $U = 0.5(u_{r,\max} - u_{r,\min})$ is velocity amplitude, ω is radian frequency, r is a non-linearity parameter and ϕ is a shape parameter. The flow is sinusoidal when $r = 0$, purely velocity-skewed when $r \neq 0$ and $\phi = -\frac{\pi}{2}$, and purely velocity-asymmetric (acceleration-skewed) when $r \neq 0$ and $\phi = 0$; other (r, ϕ) combinations lead to mixed skewed-asymmetric flows. Velocity skewness and asymmetry are calculated from

$$u_{\text{sk}} = \frac{\overline{u^3}}{(u_{\text{rms}})^3}, u_{\text{asy}} = -\frac{\overline{\mathcal{H}(u)^3}}{(u_{\text{rms}})^3} \quad (2)$$

where u_{rms} is the root-mean-square value of $u(t)$, $\mathcal{H}(u)$ is the Hilbert transform of $u(t)$ and the overline denotes time-average.

115 The modulated flows are produced by applying modulation functions to $u_r(t)$. The flow is symmetrically modulated using

$$u_m(t) = \frac{1}{\sqrt{1 + \frac{M^2}{2}}} \left(1 + M \sin \frac{2\pi t}{nT} \right) u_r(t) \quad (3)$$

where n is the number of flow periods contained within a modulated group and M is the strength of the modulation; the denominator $\sqrt{1 + \frac{M^2}{2}}$ makes the rms value of $u_m(t)$ equal to the rms of $u_r(t)$. The modulation can be made “front-leaning” (higher flows occurring early in the group) or “back-leaning” (higher flows occurring late in the group) using the sawtooth function of Malarkey & Davies (2012):

$$u_m(t) = \frac{1}{\sqrt{1 + \frac{M^2}{2}}} \left(1 + M \frac{\arctan \frac{b \sin \frac{2\pi t}{nT}}{1 - b \cos \frac{2\pi t}{nT}}}{\arctan(b(1 - b^2))^{-0.5}} \right) u_r(t) \quad (4)$$

125 $b > 0$ and $b < 0$ result in a front-leaning and a back-leaning modulation respectively. The skewness and asymmetry of $u_m(t)$ are close to the skewness and asymmetry of the corresponding $u_r(t)$ and can be made equal by slight tuning

of r and ϕ . In this way we generated corresponding regular and modulated oscillatory flows that have closely similar values of T , u_{rms} , u_{sk} and u_{asy} .

Table 1: Experimental conditions

i.d.	d_{50} (mm)	T (s)	T_g (s)	$u_{\infty,\text{rms}}$ (m/s)	$u_{\infty,\text{max}}$ (m/s)	$u_{\infty,\text{min}}$ (m/s)	$u_{\infty,\text{sk}}$ (-)	$u_{\infty,\text{asy}}$ (-)
CSSR	0.46	6	-	0.69	0.94	-0.96	-0.04	0.05
CSSS	0.46	6	60	0.69	1.53	-1.58	-0.05	0.06
CSVr	0.46	6	-	0.56	0.96	-0.61	0.42	0.10
CSVs	0.46	6	60	0.57	1.41	-0.98	0.43	0.12
CSVF	0.46	6	60	0.56	1.40	-0.99	0.44	0.12
CSVb	0.46	6	60	0.57	1.41	-0.99	0.43	0.11
CSAR	0.46	6	-	0.56	0.78	-0.78	-0.02	0.41
CSAS	0.46	6	60	0.56	1.29	-1.29	0.00	0.42
GVVR	5.65	6	-	0.56	0.96	-0.61	0.42	0.10
GVVS	5.65	6	60	0.58	1.44	-0.99	0.45	0.11

130 The test conditions are summarised in Table 1. The following four-character i.d. code is used: the first two characters indicate the bed type: “CS” = sand-rough, “GV” = gravel-rough; the third character denotes flow shape: “S” = sinusoidal, “V” = skewed, “A” = asymmetric; the fourth character denotes the modulation type: “R” = no modulation (i.e. regular flow), “S” = symmetric modulation, “F” = front-leaning modulation and “B” = back-leaning modulation. The flow period was set at $T = 6$ s and modulations contained $n = 10$ flow periods, giving a group period $T_g = nT = 60$ s. b was set at 0.7 and -0.7 to give a strong degree of leaning in the front-leaning and back-leaning modulations respectively. Figure 2 shows the free-stream velocities, $u_{\infty}(t)$, for the 5 modulated flows measured at 250 mm above the sand-rough bed. The free-stream
140 flow parameters $u_{\infty,\text{rms}}$, $u_{\infty,\text{max}}$, $u_{\infty,\text{min}}$, $u_{\infty,\text{sk}}$ and $u_{\infty,\text{asy}}$ reported in Table 1 were obtained from the measured velocities, phase-averaged over 50 flow periods in the case of the regular flows and over 50 flow groups in the case of the

modulated flows.

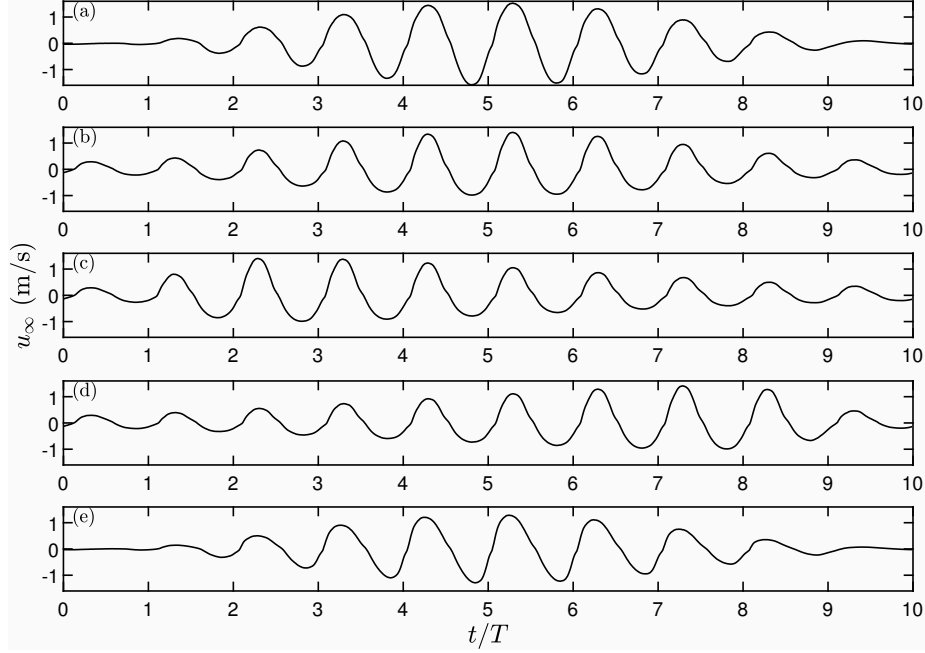


Figure 2: Measured $u_\infty(t)$ for (a) CSSS, (b) CSVS, (c) CSVF, (d) CSVB, (e) CSAS.

Figure 3 places the present experiments in $Re - a/k_s$ space. For the modulated flow experiments in which a and u vary with each half-cycle, we calculate Re and a/k_s for each half-cycle using the half-cycle peak velocity, u_{pk} , for u and half-cycle a calculated from $a = u_{pk}/\omega$; k_s is determined as described in Section 2.4. The dashed lines in Figure 3 show the $Re - a/k_s$ space covered by the flow half-cycles with $u_{pk} \geq 0.1$ m/s for the two bed types. For the gravel-rough experiments, the hydraulic conditions extend from rough turbulent for the high-velocity flow half-cycles to very rough turbulent for the lower-velocity half-cycles; for the sand-rough experiments, the hydraulic conditions are transitional for the low-velocity half-cycles, become smooth turbulent at the higher velocities and are close to rough turbulent at the very highest velocities.

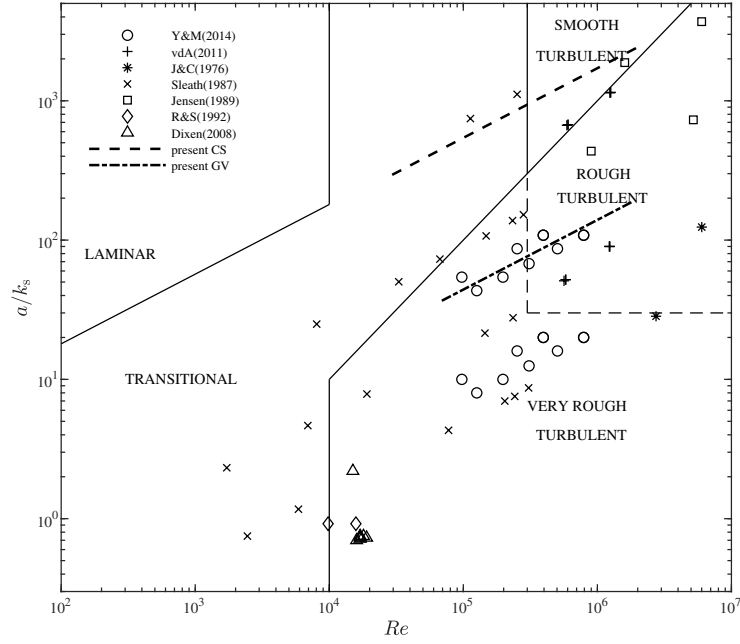


Figure 3: Hydraulic regime for present CS and GV experiments. Legend: Yuan & Madsen (2014), van der A et al. (2011), Jonsson & Carlsen (1976), Sleath (1987), Jensen et al. (1989), Ranasoma & Sleath (1992), Dixen et al. (2008)

2.3. Velocity measurement

Simultaneous horizontal and vertical velocities were measured using a Dantec FiberFlow 2-Component LDA system, comprising a 300 mW Argon-ion laser and a P60 Burst Spectrum Analyser. The probe was mounted on a computer-controlled traverse with 0.6 m range of motion in the x , y and z directions and a positioning accuracy of $10 \mu\text{m}$ (confirmed in a previous study using a confocal chromatic displacement sensor (van der A et al., 2018)). The LDA probe was fitted with a 500 mm focal length lens resulting in an ellipsoidal measurement volume that is $76 \mu\text{m}$ in diameter and approximately 1.4 mm long (i.e. 1.4 mm in the y direction, transverse to the main flow direction). The seeding was $5 \mu\text{m}$ PA-12 polyamide nylon particles with specific gravity 1.01. Data capture rates up to 800 Hz were achieved in the free-stream, while close to the bed,

where velocities are lower, data rates were typically in the range 50 to 150 Hz, depending mainly on flow phase.

170 The velocity measurements were made at a position on the tunnel's longitudinal centreline. The traverse was used to find an x position at which the laser was able to touch the top of the grain at that position without being blocked by protruding grains located between the tunnel side-wall and the measurement point. This resulted in the measurement position being at the location of a
 175 grain whose top surface is slightly higher than the surrounding grains. Using the traverse, the laser was incrementally lowered to the bed in $12.5\ \mu\text{m}$ steps until it touched the grain (detected by a high-noise signal): this position corresponds to $z_m = 0$ for the measurements. The first measurement position above the grain was obtained by incrementally raising the laser above the grain until
 180 a good signal was obtained.

For the sand-rough bed, velocities were measured at approximately 40 elevations along a single vertical line (i.e. fixed x position), with the lowest measurement at $z_m = 40$ or $50\ \mu\text{m}$ (depending on flow condition) above the grain crest and the highest measurement well into the free-stream at $z_m = 250\ \text{mm}$. The
 185 measurement positions were logarithmically spaced, with a vertical separation of 0.01 or 0.02 mm between the lowest two positions and a vertical separation of 35 to 50 mm between the two highest positions; 11 to 15 measurements were made within 1 mm of the grain crest. For the gravel-rough bed, measurements were again made at approximately 40 elevations above the bed, between
 190 $z_m = 70\ \mu\text{m}$ and $z_m = 209\ \text{mm}$. The bottom two measurement elevations had a vertical separation of $30\ \mu\text{m}$ and the highest two elevations had a separation of 34.23 mm (for GVVR) or 28.6 mm (for GVVS); there were 8 measurement elevations within 1 mm of the grain crest. To account for spatial non-homogeneity in the flow in the near-bed region due to the large grains, measurements were
 195 made at several x positions for elevations close to the gravel-rough bed. The x positions were spaced 1 mm apart and the number reduced with increasing height above the bed: for GVVR, there were 15 x positions at the lowest 4 elevations ($z_m = 70, 100, 140, 200\ \mu\text{m}$), gradually reducing to one x position

for $z_m > 100$ mm; for GVVS, there were 5 x positions at the lowest 9 elevations
 200 $(0.05 \text{ mm} \leq z_m \leq 1.166 \text{ mm})$, decreasing to one x position for $z_m > 32.23$ mm.

Following a period longer than about 200 flow cycles to fully establish the hydrodynamics within the tunnel (and to evacuate air bubbles and disperse seeding), velocity measurements were made over 50 flow periods ($50T$) in the case of the regular flows and over 50 flow groups ($50T_g$) in the case of the modulated
 205 flows. Velocity measurements were phase-locked by synchronously recording a once-per-cycle pulse from the piston control with the velocity measurements. Phase averaging was carried out using a temporal bin size $\Delta t = 1/15$ s. Data values outside ± 6 standard deviations from the mean of the data in the bin were identified as spikes and discarded; the average velocity for the bin was taken as
 210 the weighted average of the de-spiked data, with the weighting based on seeding particle transit time across the measurement volume. Averaging over multiple flow cycles, and, in the case of the gravel-rough bed, across multiple x positions, the phase-averaged horizontal velocity is obtained from

$$\langle \hat{u} \rangle(z, t) = \frac{\sum_{p=1}^P \sum_{n=1}^N \sum_{m=1}^M u_m(x_p, z, \phi + (n-1)T') tt_m(x_p, z, \phi + (n-1)T')}{\sum_{p=1}^P \sum_{n=1}^N \sum_{m=1}^M tt_m(x_p, z, \phi + (n-1)T')}, 0 \leq t < T' \quad (5)$$

215 where $T' = T$ for the regular flows and $T' = T_g$ for the modulated flows, ϕ is the phase bin $t \leq \phi < (t + \Delta t)$, M is the number of measurements of u within a phase bin, tt is seeding residence time (measured by the LDA), $N = 50$ is the number of flow cycles and P is the number of x measurement locations for given z ($P = 1$ for the sand-rough experiments and $P = 1$ to 15, depending
 220 on z , for the gravel-rough experiments); angle brackets and circumflex denote phase-average and spatial-average respectively.

Mean square turbulent fluctuations in u are calculated from

$$\widehat{\langle u'^2 \rangle}(z, t) = \frac{\sum_{p=1}^P \sum_{n=1}^N \sum_{m=1}^M (u_m(x_p, z, \phi + (n-1)T' - \langle \hat{u} \rangle(z, t)))^2 tt_m(x_p, z, \phi + (n-1)T')}{\sum_{p=1}^P \sum_{n=1}^N \sum_{m=1}^M tt_m(x_p, z, \phi + (n-1)T')} \quad (6)$$

Similar equations to Equations 5 and 6 can be written for $\langle \hat{w} \rangle(z, t)$ and $\widehat{\langle w'^2 \rangle}(z, t)$.
 225 The phase-averaged turbulent (Reynolds) **kinematic** stress, $\widehat{\langle u'w' \rangle}(z, t)$ (simply called turbulent stress in what follows) is calculated using Equation 6 with $(u_m(x_p, z, \phi + (n-1)T' - \langle \hat{u} \rangle(z, t)))^2$ replaced by $u_m(x_p, z, \phi + (n-1)T' - \langle \hat{u} \rangle(z, t))w_m(x_p, z, \phi + (n-1)T' - \langle \hat{w} \rangle(z, t))$. For the remainder of the paper: we write $u(z, t)$ and $w(z, t)$ (or simply u and w) for the phase-averaged velocities
 230 $\langle \hat{u} \rangle(z, t)$ and $\langle \hat{w} \rangle(z, t)$ respectively; $u'_{\text{rms}}(z, t)$ and $w'_{\text{rms}}(z, t)$ are the root-mean-square turbulent fluctuations $\sqrt{\widehat{\langle u'^2 \rangle}}$ and $\sqrt{\widehat{\langle w'^2 \rangle}}$ respectively; and we write $u'w'(z, t)$ for the phase-averaged turbulent stress $\widehat{\langle u'w' \rangle}(z, t)$.

The 2-d LDA measurements yield the u'_{rms} and w'_{rms} contributions to the total turbulent kinetic energy per unit mass, k . The v'_{rms} contribution is expected
 235 to lie approximately mid-way between u'_{rms} and w'_{rms} (Soulsby, 1983; Svendsen, 1987; Justesen, 1991). Here we use the component ratios from Soulsby (1983) to estimate k :

$$k = 1.481 \times \frac{1}{2} ((u'_{\text{rms}})^2 + (w'_{\text{rms}})^2) \quad (7)$$

The wider collection of data from Soulsby (1983) suggests the scaling ratio lies
 240 between 1.4 and 1.5, which provides an uncertainty estimate of -5% to 1% on k calculated from Equation 7.

2.4. Hydraulic roughness

Bed roughness for the sand-rough bed was determined by fitting a logarithmic profile for rough turbulent flow to vertical profiles of u for selected times in

the flow. With velocities measured at heights z_m , the log-profile referenced to displacement d' below this height (Figure 4) is

$$\frac{u}{u_*} = \frac{1}{\kappa} \ln \frac{z_m + d'}{z_0} \quad (8)$$

where $u = u(z_m, t)$ is the phase-averaged velocity at selected time t and measurement height z_m , u_* is the instantaneous shear velocity ($u_* = \sqrt{\tau_0/\rho}$, τ_0 = bed shear stress, ρ = water density), $\kappa = 0.4$ is von Kármán's constant and z_0 is the vertical position of zero (mean) velocity.

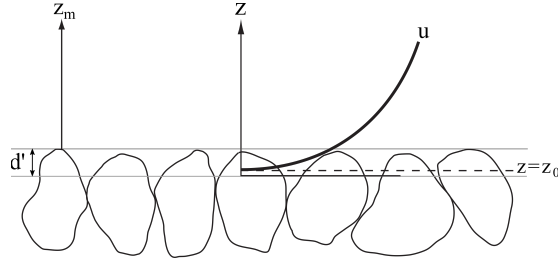


Figure 4: Definition sketch for z , z_m , z_0 and d'

According to Jackson (1981), d' is correctly interpreted as the height at which the average drag on the surface appears to act. In other words, d' is more than a fitting parameter used to optimise log-profile fits. The zero (mean) velocity level can be no higher than the grain tips, which means d' must be greater than $z_0 \approx d_{50}/12$. Based on Jackson's Table 1 for sand and gravel, d' should be less than $0.35d_{50}$, implying the zero velocity level must be less than $0.35d_{50} - d_{50}/12 = 0.27d_{50}$ below the grain tips. For the present fitting, we constrain d' to lie in the range $(0.15 - 0.35)d_{50}$ and, following Davies (1986), we fit a straight line to $(u, \ln(z_m + d'))$ data in the region $0.2k_s < z_m < 0.2\delta$, where δ is distance from the grain tips to the peak in the velocity profile (the velocity overshoot) and k_s is initially estimated to be $2.5d_{50}$. The upper limit $z_m = 0.2\delta$ is slightly higher than the upper limit of the log region suggested by Davies (1986), but is significantly lower than that taken in other studies (e.g.

van der A et al., 2011). The slope of the straight line, m , gives the shear velocity $u_* = \kappa/m$, and the line's intercept with $u = 0$, c , gives the roughness height $z_0 = e^c$; the equivalent Nikuradse roughness is then $k_s = 30z_0$.

Two vertical profiles of u were analysed for each of the eight sand-rough experiments, one profile corresponding to the phase of maximum positive free-stream velocity, $u_{\infty, \max}$, the other corresponding to the phase of maximum negative free-stream velocity $u_{\infty, \min}$. For each profile, the log-fit analysis was carried out for five values of d'/d_{50} (0.15, 0.2, 0.25, 0.3, 0.35), giving 80 fits in total (8 flows \times 2 profiles \times 5 d'/d_{50}). Example fits are shown in Figure 5. There were approximately 10 data points in each fit and the normalised mean square error almost always exceeded 0.95.

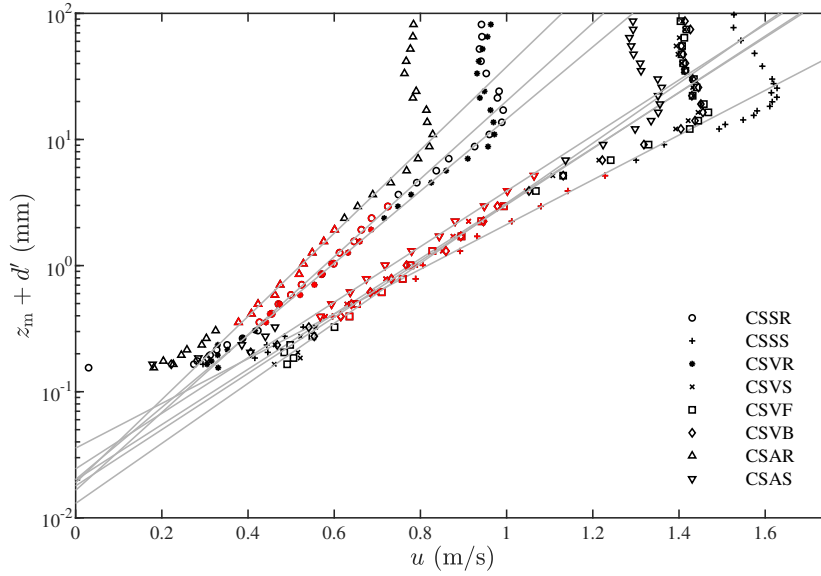


Figure 5: Example log-profile fitting for CS experiments: the velocity profiles correspond to $u_{\infty, \max}$; data points included in fit are shown in red; grey lines are fits with $d' = 0.25d_{50}$.

Figure 6 shows the values of k_s/d_{50} obtained from the 80 fits. There is wide variation in the 16 values obtained at each d'/d_{50} , the highest k_s/d_{50} being approximately 3 times the lowest value. While the highest value of k_s/d_{50} at each d'/d_{50} happens to come from the experiment with the highest of the

16 velocity magnitudes (CSSS, Figure 5), close analysis showed no systematic dependence of k_s/d_{50} on velocity magnitude (or Re). k_s/d_{50} increases with increasing d'/d_{50} : for each flow, the highest k_s/d_{50} , which occurs for $d'/d_{50} = 0.35$, is approximately 1.6 times the lowest k_s/d_{50} , which occurs for $d'/d_{50} = 0.15$. The average of all estimates of k_s/d_{50} is 1.3, indicated by the dashed line in Figure 6. Based on this analysis, we take $k_s = 1.3d_{50}$ with $d' = 0.25d_{50}$ as the best estimate of the CS bed roughness.

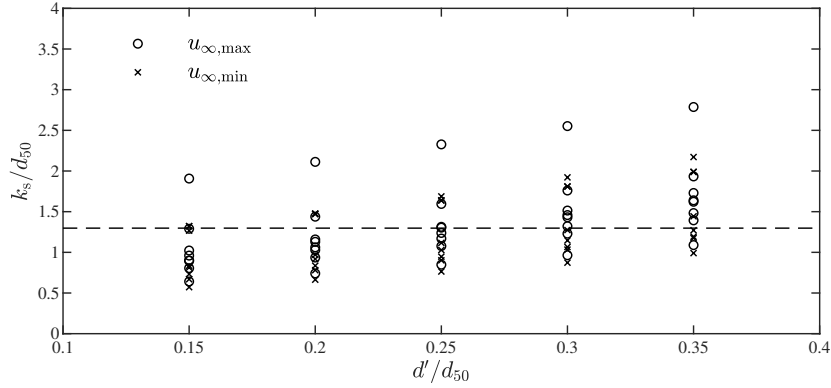


Figure 6: k_s/d_{50} dependence on d'/d_{50} from log-fitting to CS velocity profiles at phase of maximum positive (o) and maximum negative (x) free-stream velocity; dashed line: $k_s/d_{50} = 1.3$

Based on particle image velocimetry measurements in velocity-asymmetric oscillatory flows, van der A et al. (2011) estimated $k_s = 2.38d_{50}$ for a similar sand-rough bed to that used in the present study. The large difference between the van der A et al. estimate and $k_s = 1.3d_{50}$ from the present experiments is explained by the different methods used in the log profile fitting. van der A et al. (2011) fitted to vertical profiles of the amplitude of the first harmonic of measured velocity, whereas in the present study we more correctly fit to the vertical profiles of instantaneous velocity. Applying the van der A et al. (2011) approach to the CS flows of the present study, for five values of d'/d_{50} , gives an average $k_s = 2.7d_{50}$, which is reasonably close to the van der A et al. value. Similar to the results shown in Figure 6, fitting to the profiles of velocity first

harmonic amplitude also shows k_s/d_{50} increasing with increasing d'/d_{50} and a factor ~ 3 difference between the highest and lowest k_s for each d'/d_{50} .

300 The GV experiments have significantly lower a/k_s than the CS experiments, which means the log-layer is contained within a tighter range of z_m/k_s (Davies, 1986). The flow region $0.2k_s < z_m < 0.2\delta$ for GVVR and GVVS contains only one or two data points, which means we cannot apply log-profile fitting to determine k_s . For this reason we pragmatically assume that the $k_s = 1.3d_{50}$
 305 obtained from the CS experiments applies also to the GV experiments. There is some support for this approach: the estimate is close to the $k_s = 1.4d_{50}$ reported by Fuhrman et al. (2010) from steady flow [experiments](#) over a fixed bed of 7 mm pebbles.

3. RANS model

310 The experimental data are compared with predictions from a 1DV Reynolds-averaged Navier Stokes (RANS) model with $k - \epsilon$ turbulence closure. The momentum equation for high-Re, wave-current flow in the x direction, with zero vertical wave velocity, is

$$\frac{\partial u}{\partial t} = -\frac{1}{\rho} \frac{\partial p}{\partial x} + \frac{\partial}{\partial z} \left(\nu_t \frac{\partial u}{\partial z} \right) \quad (9)$$

315 where ρ is the fluid density and ν_t is the eddy viscosity. $\frac{\partial p}{\partial x}$ is the horizontal pressure gradient given by $\frac{\partial p}{\partial x} = \frac{\partial \bar{p}}{\partial x} - \rho \frac{\partial u_\infty}{\partial t}$, where \bar{p} is the mean pressure (associated with any steady current that is present).

The balance equation for turbulent kinetic energy, k , is

$$\frac{\partial k}{\partial t} = \frac{\partial}{\partial z} \left(\frac{\nu_t}{\sigma_k} \frac{\partial k}{\partial z} \right) + \nu_t \left(\frac{\partial u}{\partial z} \right)^2 - \epsilon \quad (10)$$

320 where terms on the right hand side denote turbulence diffusion, production and dissipation respectively, and σ_k is a turbulence closure constant.

The equation for turbulent kinetic energy dissipation rate, ϵ is

$$\frac{\partial \epsilon}{\partial t} = \frac{\partial}{\partial z} \left(\frac{\nu_t}{\sigma_\epsilon} \frac{\partial \epsilon}{\partial z} \right) + C_{\epsilon 1} \frac{\epsilon \nu_t}{k} \left(\frac{\partial u}{\partial z} \right)^2 - C_{\epsilon 2} \frac{\epsilon^2}{k} \quad (11)$$

where $\nu_t = C_\mu k^2 / \epsilon$ and the values for the constants C_μ , $C_{\epsilon 1}$, $C_{\epsilon 2}$, σ_ϵ and σ_k are
 325 0.09, 1.44, 1.92, 1.00 and 1.3 respectively, as given by Rodi (1993).

Equation 9 is subject to the no-slip boundary condition at the bottom, $u(z_0, t) = 0$, and a no-shear condition on the upper boundary, $\frac{\partial u(h, t)}{\partial z} = 0$. In the near-bed region the Reynolds stresses are nearly constant, convection and diffusion of k are negligible, and, therefore, k production is balanced by k
 330 dissipation. It follows from Equations 10 and 11 that $k(z_0, t) = u_*^2 / \sqrt{C_\mu}$ and $\epsilon(z_0, t) = u_*^3 / (\kappa z_0)$. At the upper boundary, $\frac{\partial k(h, t)}{\partial z} = 0$ and $\frac{\partial \epsilon(h, t)}{\partial z} = 0$.

Asymmetry in turbulence intensity and, therefore, in eddy viscosity between successive half-cycles of non-symmetric oscillatory flow gives rise to a time-averaged forcing term in the equation of motion. This acts in an analogous
 335 way to a steady horizontal pressure gradient and has the effect of generating a steady current. However, unlike a pressure gradient term that is normally assumed to have the same effect at all heights within the boundary layer, this additional forcing term is strongly height-dependent. If the horizontal velocity, eddy viscosity and pressure forcing term, $P_x = -\frac{1}{\rho} \frac{\partial p}{\partial x}$, are expressed as the sum
 340 of a time-averaged component (overbar) and a periodic component (tilde),

$$u = \bar{u} + \tilde{u} \quad \nu_t = \bar{\nu}_t + \tilde{\nu}_t \quad P_x = \bar{P}_x + \tilde{P}_x \quad (12)$$

then the following time-averaged equation of motion is obtained from Equation 9:

$$0 = \bar{P}_x + \frac{\partial}{\partial z} \left(\bar{\nu}_t \frac{\partial \bar{u}}{\partial z} \right) + \frac{\partial}{\partial z} \left(\overline{\tilde{\nu}_t \frac{\partial \tilde{u}}{\partial z}} \right) \quad (13)$$

345 The three terms on the right-hand side of Equation 13 represent, respectively,

any steady pressure forcing that may be present, diffusion of the cycle-mean momentum and a forcing whose magnitude depends on the phase relationship between the periodic components of the eddy viscosity and velocity gradient. Only if these terms are in quadrature will this term be zero at a given height. In
350 skewed and asymmetric flows, the extra forcing term is found from the model to be negative near the bed, to decrease in magnitude away from the bed and, as expected, to tend to zero at the edge of the oscillatory boundary layer. In the absence of a steady pressure gradient (i.e. $\bar{P}_x = 0$, as assumed for symmetric flows), this implies that the second term on the right-hand side of Equation
355 13, involving time-averaged quantities, is positive near the bed and decreases upwards. This results in the generation of a residual current in the negative x direction at all levels, satisfying the bottom boundary condition $\bar{u} = 0$ at $z = z_0$ and reaching a constant negative value above the oscillatory boundary layer. A negative flow at all levels cannot, of course, occur in a flow tunnel with
360 a rigid lid at the top and walls on either side. If a mean negative current is generated in the bottom boundary layer, a compensating positive return flow must exist higher up from the bed. The question arises how best to represent this residual current in the model. Following Davies & Li (1997), the procedure adopted here is to apply an opposing, positive mean pressure force term \bar{P}_x in
365 the model, having a magnitude that causes the predicted residual current to be zero at the same height within the boundary layer where the measured residual current is zero. Above this height the measured residual is influenced by tunnel effects and the model simply allows the residual to increase towards a maximum value at the upper boundary $z = h$. The model-experiment comparisons that
370 follow are therefore only meaningful in the near-bed region.

Equations 9, 10 and 11 were solved subject to the specified boundary conditions on a log-linear vertical grid comprising 65 vertical levels between $z = z_0$ and $z = h$, with an assumed water depth $h = 1$ m (i.e. about twice the actual water depth in the AOFT). Based on the hydraulic roughness analysis (Sec-
375 tion 2.4), the roughness height is taken to be $z_0 = k_s/30 = 1.3d_{50}/30$, giving $z_0 = 0.02$ mm for CS and $z_0 = 0.245$ mm for GV. Each simulation involved 180

time steps per 6-second flow period and calculations were carried out for 200 flow periods to ensure convergence. For each flow case, the model was forced by applying at $z = h$ the time-varying pressure gradients derived from the oscillatory component of the phase-averaged measured free-stream velocity plus a mean pressure force that results in the residual current being zero at the same z where the measured residual is zero, as described above. For model-experiment comparisons, model z corresponds to $z_m + d'$, where d' is $0.25d_{50} = 0.115$ mm for CS and 1.412 mm for GV.

4. Results

Experimental and model results are presented in three main sections: phase-averaged velocities; turbulent kinetic energy; turbulent stress and bed shear stress.

4.1. Phase-averaged velocities

Figure 7 shows vertical profiles of phase-averaged u corresponding to the time of maximum positive free-stream velocity for the 10 experiments; the figure also shows the corresponding model-predicted profiles. Approaching the bed from the free-stream, the profiles show an overshoot region where velocities exceed the free-stream velocity, followed by decreasing velocity as the bed is approached. For CS the peak overshoot velocity occurs at between 10 and 20 mm from the bed, depending on the flow case, while for GV the peak overshoot is higher at between 20 and 30 mm. The CSVS, CSVF and CSVB profiles, which have similar $u_{\infty, \max}$ and similar flow shape, overlap each other well, indicating that the profile is not affected by the positioning of the flow half-cycle containing $u_{\infty, \max}$ relative to the other flow half-cycles within the modulated flow group. The model-predicted profiles show good agreement with the measurements in terms of profile shape and magnitude of peak overshoot velocity. The predicted peak overshoot z positions and velocities within the boundary layer are in better agreement with the measurements for GV than for CS. In the case of CS, the

405 model tends to predict slightly higher z for the overshoot peak and generally
lower velocities within the boundary layer compared with the measurements, the
difference between model and measured being greater in the case of the regular
flow profiles, which have lower $u_{\infty, \max}$ and are less turbulent than $u_{\infty, \max}$ of the
modulated flows. The better agreement between model and measured for GV
410 than for CS, and for higher velocities in CS, is likely due to the assumption of
rough turbulent flow inherent in the model. In reality, the flow is rough turbulent
for GV but is not quite rough turbulent for CS, even under the highest velocities
of the modulated flows.

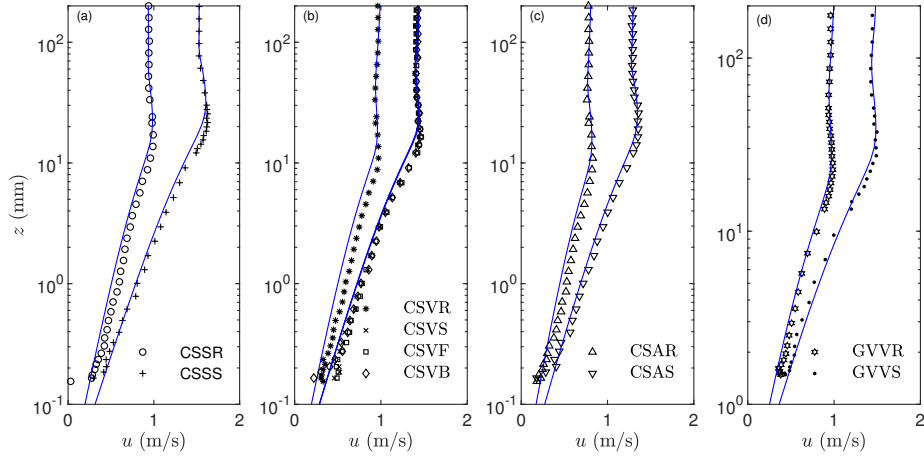


Figure 7: $u(z)$ at phase corresponding to $u_{\infty, \max}$ for the CS (a-c) and GV (d) experiments; corresponding model-predicted $u(z)$ are shown in blue; in panel (b), the model results for CSVS, CSVF and CSVB overlie one another.

Boundary layer thickness

415 The height of the peak overshoot velocity at the phase of maximum free-
stream velocity, δ , is often used as a measure of oscillatory flow boundary layer
thickness. Measures of δ were obtained for flow half-cycles having $u_{pk} \geq 0.5$
m/s. This gave 2 measures of δ from each of the regular flow experiments (one
corresponding to peak positive velocity and one corresponding to peak negative
420 velocity) and between 10 and 12 measures from each of the modulated flow

experiments. The experimental results are presented in Figure 8(a), showing δ/k_s plotted against a/k_s . Here a is calculated for each flow half-cycle taking account of flow shape, i.e. $a = 4t_{pk}u_{pk}/(2\pi)$, where t_{pk} is the time from flow reversal to the time when $u_\infty = u_{pk}$. The corresponding model-predicted δ are presented in Figure 8(b). The results in Figure 8 are shown with reference to Fredsøe & Deigaard (1992)'s formula for rough-turbulent δ , slightly modified by van der A et al. (2011):

$$\frac{\delta}{k_s} = 0.075 \left(\frac{a}{k_s} \right)^{0.82} \quad (14)$$

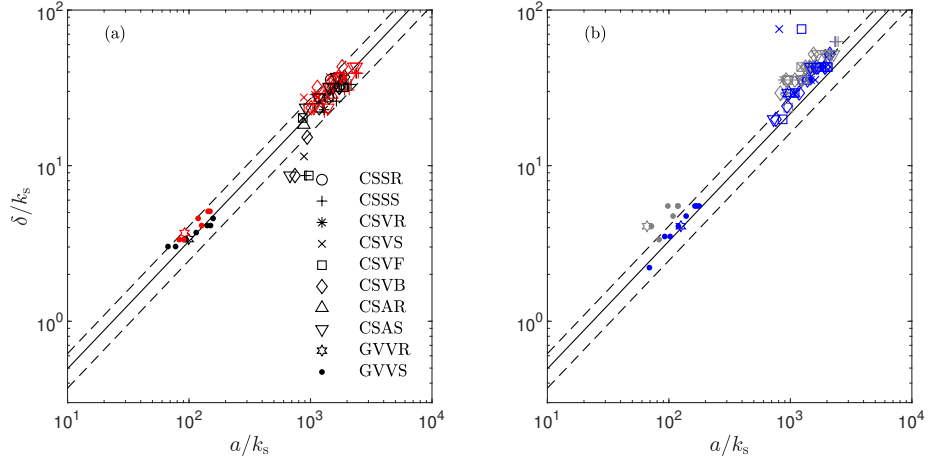


Figure 8: δ/k_s versus a/k_s for flow half-cycles with $u_{pk} \geq 0.5$ m/s. (a): experimental results for positive (black) and negative (red) flow half-cycles; (b) model predictions for positive (blue) and negative (grey) flow half-cycles. Solid line is Equation 14 and dashed lines are $\pm 25\%$ of Equation 14.

Figure 8(a) shows generally good agreement between the CS experimental data and the van der A et al. (2011) formula. The few results that show poor agreement correspond to $a/k_s < 10^3$, for which the flow is not fully turbulent (Figure 3). For GV there is also generally good agreement between the experimental data and the formula, although the formula tends to underestimate δ somewhat for the negative flow half-cycles in these cases. Note that the general

good agreement between the experimental results and the van der A et al. (2011)
 435 formula seen in Figure 8(a) cannot be taken as validation of the k_s estimated
 from the log-profile fitting because δ is weakly dependent on k_s ($\delta \propto k_s^{0.18}$).
 Figure 8(b) shows δ from the model-predicted velocity profiles. The tendency
 seen in Figure 7 for the model to give higher δ than the experiments is evident
 by comparing Figure 8(b) with Figure 8(a). The over-prediction is typically
 440 $\sim 35\%$.

Phase lead

Velocity within the boundary layer increasingly leads the free-stream velocity
 as the bed is approached from the free-stream. We estimate the phase lead, ϕ , at
 each z through the boundary layer by calculating the phase difference between
 445 the first harmonic of $u(z, t)$ and $u_\infty(t)$. The results from the 10 experiments
 are shown in Figure 9(a). Here z is normalised by a “representative” δ , δ_r ,
 calculated using Equation 14 with a based on the root-mean-square value of
 $u_\infty(t)$, i.e.

$$\frac{\delta_r}{k_s} = 0.075 \left(\frac{a_{\text{rms}}}{k_s} \right)^{0.82} \quad (15)$$

450 where $a_{\text{rms}} = \sqrt{2}u_{\infty, \text{rms}}/\omega$. (The values of a_{rms} and δ_r for the 10 experiments
 are given in Table 2.) Figure 9(a) shows good agreement in $\phi(z)$ magnitude
 and profile shape across all CS experiments, at least for $z/\delta_r > \sim 0.05$, which is
 above approximately two grain diameters from the bed. $\phi(z)$ is slightly negative
 for z/δ_r between ~ 5 and ~ 2 because velocity amplitude is slightly higher than
 455 the free-stream velocity amplitude in this region. Moving downwards, velocity
 amplitude decreases through the boundary layer, which means the flow responds
 sooner to the change in pressure gradient and $\phi(z)$ becomes increasingly positive,
 reaching a maximum value of between 15° and 18° at $z/\delta_r \approx 0.05$ (approximately
 0.8 mm above the bed). Below this level, the regular flow cases (CSSR, CSVr
 460 and CSAR) show a decrease in ϕ as the bed is approached, while the modulated
 flows tend to hold the value of ϕ reached at $z/\delta_r \approx 0.05$ because of their higher

velocities. The GV results show similar profile characteristics to CS, but the maximum value reached is significantly higher because of the thicker boundary layer and lower velocities compared to CS, reaching $\sim 27^\circ$ close to the bed.

465 The model results for $\phi(z)$ are in general good agreement with the experimental results both in terms of profile shape and magnitude, for both CS and GV. For the model, ϕ increases all the way to $z = z_0$ but reaches about 95% of its maximum value by $z/\delta_r \approx 0.05$.

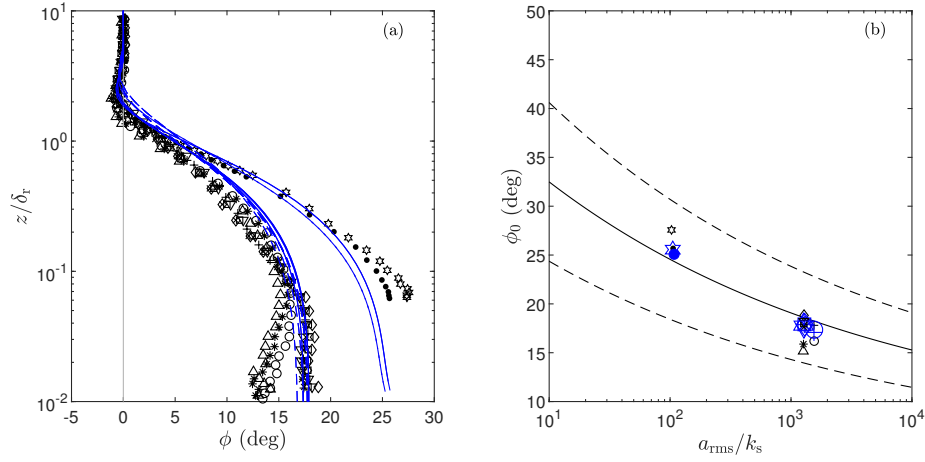


Figure 9: Experimental and model-predicted (a) $\phi(z)$ and (b) ϕ_0 ; symbols are the same as previous figures; solid/dashed blue lines in (a) are model results for regular/modulated flows; solid line in (b) is Equation 16 and dashed lines are $\pm 25\%$ of ϕ_0 from Equation 16; model (blue) results in (b) are magnified for clarity.

470 Figure 9(b) shows the experimental and model values of maximum phase lead, ϕ_0 , occurring at or very near the bed, plotted as a function of a_{rms}/k_s . The results are shown with reference to the formula for phase lead of bed shear stress attributed to Humbyrd (2012), as reported in Yuan & Madsen (2014). Here, we write the formula in terms of a_{rms} :

$$\phi_0^\circ = \frac{180}{\pi} \left(0.649 \left(\frac{a_{rms}}{k_s} \right)^{-0.16} + 0.118 \right) \quad (16)$$

475 The experimental results are generally lower than the formula at high a_{rms}/k_s (the CS cases) and slightly higher than the formula at lower a_{rms}/k_s (the GV cases), but the maximum difference between experiment and formula is only 3° . Values of ϕ_0 from the model are also in good agreement with the formula.

Skewness and asymmetry

480 For non-symmetric oscillatory boundary layer flow, flow shape is known to change between free-stream and the bed (e.g. Henderson et al., 2004, Berni et al., 2013). Figure 10 shows vertical profiles of the skewness and asymmetry of u from the experiments and the model. The experimental profiles show some spurious behaviour for $z/\delta_r < \sim 0.025$ for the CS cases and $z/\delta_r < \sim 0.23$ for the
 485 GV cases, i.e. within one grain diameter above the bed for each bed type. This is likely due to the combined effect of low flow velocities and local influence of the bed on the flow this close to the bed.

As already seen in Table 1, the symmetric flow cases CSSR and CSSS (Figure 10(a) and (e)) are not exactly symmetric (the piston does not produce a
 490 perfectly sinusoidal flow): they have slight negative skewness and slight positive asymmetry. These low values barely change from free-stream through the boundary layer, except close to the bed ($z/\delta_r < \sim 0.1$) where the asymmetry increases as the bed is approached. The model results for CSSR and CSSS show essentially no change in skewness and asymmetry through the boundary layer.
 495 Consider now the skewness-dominant cases CSVr, CSVs, CSVf, CSVb (Figure 10(b) and (f)) and GVVR, GVVS (Figure 10(d) and (h)). For these cases the skewness decreases slightly for z/δ_r between ~ 5 and ~ 2 , before regaining its free-stream value at $z/\delta_r \approx 1$, and more-or-less maintaining this value through the rest of the boundary layer. These flows have very low asymmetry, which
 500 decreases to zero through the boundary layer and, in the GV cases, becomes slightly negative very close to the bed. The trends in the skewness and asymmetry profiles for these skewness-dominant flows are generally well predicted by the model. Consider next the asymmetry-dominant CSAR and CSAS cases (Figure 10(c) and (g)). For these, the high value of free-stream asymmetry is maintained

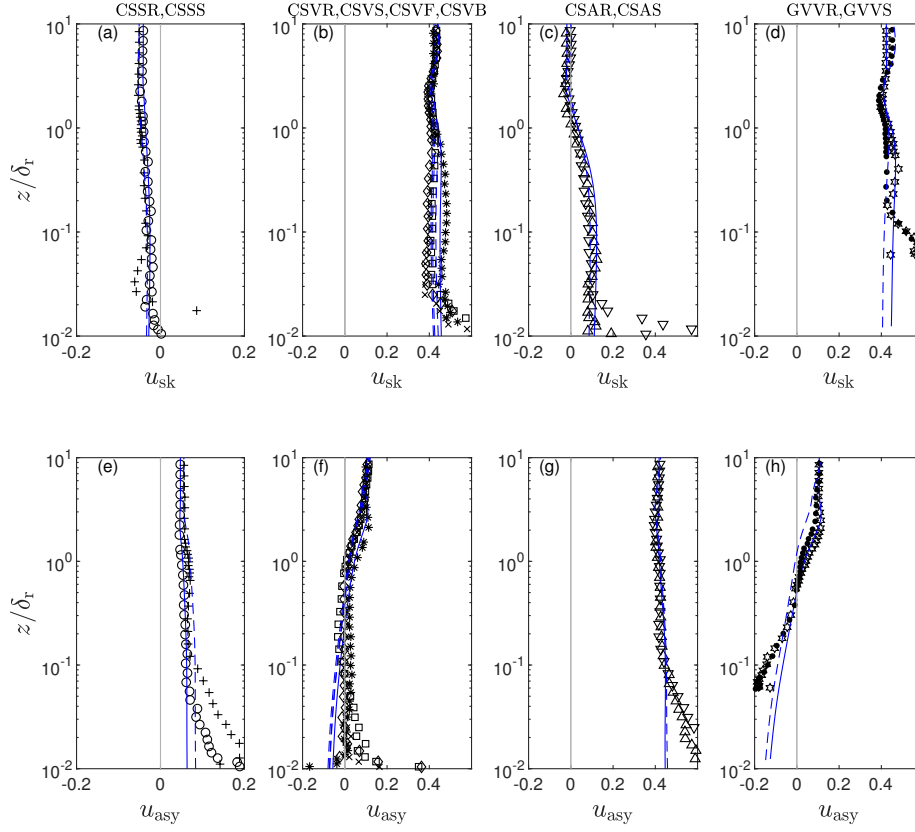


Figure 10: $u_{sk}(z)$ (a-d) and $u_{asy}(z)$ (e-h) for the 10 cases; columns and symbols are the same as in Figure 7; model predictions for regular/modulated flows are shown by solid/dashed blue lines.

505 through the boundary layer and increases close to the bed ($z/\delta_r < \sim 0.09$), similar to behaviour seen in Figure 10(e). At the same time, the skewness, which is close to zero in the free-stream, starts to increase high in the boundary layer at $z/\delta_r \approx 1.5$, and reaches a maximum value of approximately 0.1 at $z/\delta_r \approx 0.2$, which it more-or-less maintains through the remainder of the boundary layer.

510 Again, the model does well generally in predicting the skewness and asymmetry profiles, although the increase in asymmetry close to the bed seen in the experiments is not predicted by the model. The boundary layer skewness induced by free-stream asymmetry observed here is consistent with observations made

by van der A et al. (2011) and Berni et al. (2013). A significant result in the
 515 context of the present paper is that we see good agreement in skewness and
 asymmetry profiles between corresponding regular and modulated flows.

Time-averaged velocity

As described in Section 3, asymmetry in turbulence intensity between suc-
 cessive flow half-cycles, caused by asymmetry in the free-stream flow, leads to
 520 a non-zero time-averaged velocity, \bar{u} , within the boundary layer. Measurements
 and model predictions of the vertical profiles of \bar{u} are presented in Figure 11
 (note different \bar{u} range for each sub-plot). Consider first the flow profiles above
 one grain diameter from the bed, i.e. $z/\delta_r > \sim 0.025$ for CS and $z/\delta_r > \sim 0.23$
 for GV. For reasons given previously, the model results for \bar{u} are only mean-
 525 ingful below the z/δ_r where the measured \bar{u} and the matched model \bar{u} are zero
 ($z/\delta_r \approx 2 - 3$). As expected the (almost) symmetric flow cases CSSR and CSSS
 (Figure 11(a)) show near-zero \bar{u} through the boundary layer (although the ex-
 perimental data show slight positive \bar{u} within one grain above the bed). The
 skewness-dominant cases (Figure 11(b) for CS and Figure 11(d) for GV) show
 530 negative \bar{u} within the boundary layer. Profile shapes are similar for regular
 and corresponding modulated flows, but the magnitude of \bar{u} is greater for the
 regular flows. The negative peak occurs in the region $0.4 \leq z/\delta_r \leq 0.8$ and is
 approximately 50% greater in the case of the regular flow compared with the
 corresponding modulated flows. Profiles of \bar{u} for CSVS, CSVF and CSVB are
 535 very similar, implying modulation shape has no effect on \bar{u} . The asymmetric-
 dominant cases CSAR and CSAS (Figure 11(c)) also show negative \bar{u} in the
 boundary layer, but the magnitude is lower than for the skewness-dominant
 cases and, again, \bar{u} is approximately 50% higher for the regular flow compared
 with the modulated flow. The model does well overall in predicting profile shape
 540 and magnitude for all cases, including predicting higher \bar{u} for the regular flows
 compared with the modulated flows, albeit with lower difference than the $\sim 50\%$
 difference seen in the experimental results.

The experimental results show small positive \bar{u} very close to the bed for all

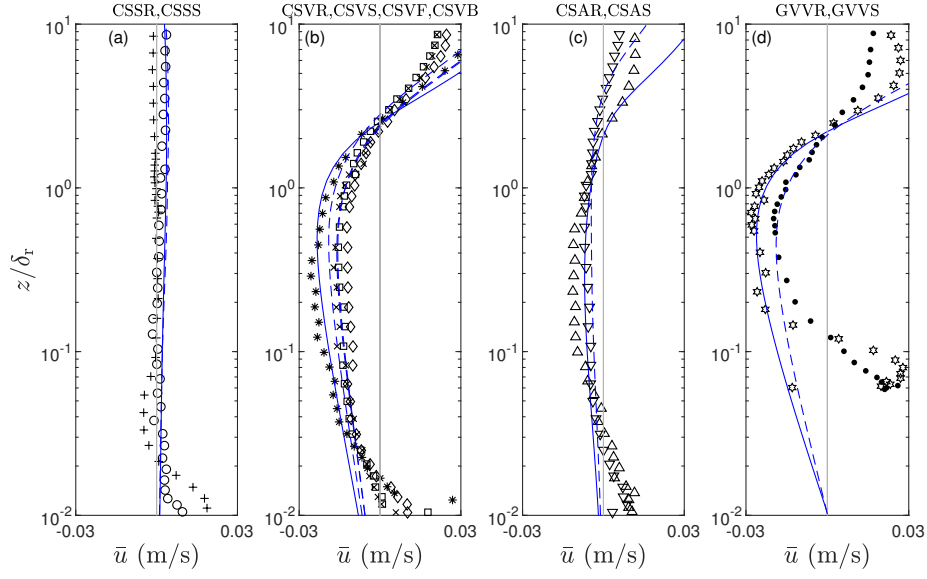


Figure 11: $\bar{u}(z)$ for the 10 cases; columns and symbols are the same as in Figure 7; model predictions for regular/modulated flows are shown by solid/dashed blue lines.

cases. It occurs below about one grain diameter ($z/\delta_r < \sim 0.025$) in the CS
 545 experiments and below about one-half a grain diameter ($z/\delta_r < \sim 0.12$) in the
 case of GV. This very near-bed positive \bar{u} is not predicted by the model because
 of the no-slip boundary condition at $z = z_0$. The cause of this streaming in the
 experiments is not certain, but may be due to flow behaviour local to individual
 grains on the bed, whereby vortices are formed more vigorously during one half-
 550 cycle than during the other, causing a change in the mean drift, as suggested
 by Sleath (1987).

4.2. Turbulent kinetic energy

Figure 12 shows measured turbulent kinetic energy, $k(z, t)$, for an example
 experiment, CSVF. Turbulence is higher under the positive flow half-cycles than
 555 under the neighbouring negative flow half-cycles, echoing the skewness in the
 free-stream flow. The turbulence is generated at the bed, then propagates and
 decays upwards with time. It decays during flow deceleration in each half-cycle,

but, as will be demonstrated more clearly below, k does not decay fully to zero by the end of the half-cycle when u_∞ is zero. Note there is little sign
560 of turbulence in the early few half-cycles of the group, even though velocity amplitude reaches almost 0.8 m/s.

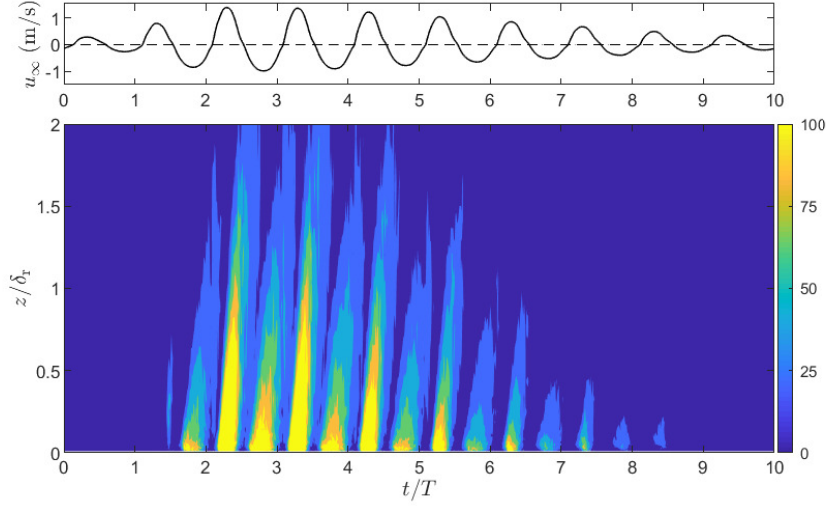


Figure 12: $k(z, t)$ (cm^2/s^2) for experiment CSVF.

Turbulence propagation

We analyse the upward propagation of k using cross-correlation to determine the lag in $k(z = z_m + d', t)$ relative to $k(z = z_{m1} + d', t)$, where z_{m1} is the
565 lowest measurement position. The $k(z, t)$ data are smoothed with a Gaussian-weighted moving-average filter with 5 data points in the window prior to the cross-correlation. The upward propagation speed, c_k , is obtained from the slope of the straight line through $(\Delta z, \Delta t)$ data points, where Δz is the elevation difference and Δt is the time lag from the cross-correlation. An example of the
570 analysis is presented in Figure 13, showing GVS, for which $c_k = 21$ mm/s.

Results for c_k for the 10 experiments are presented in Table 2. c_k is remarkably consistent across all CS experiments, with values between 13 and 15 mm/s;

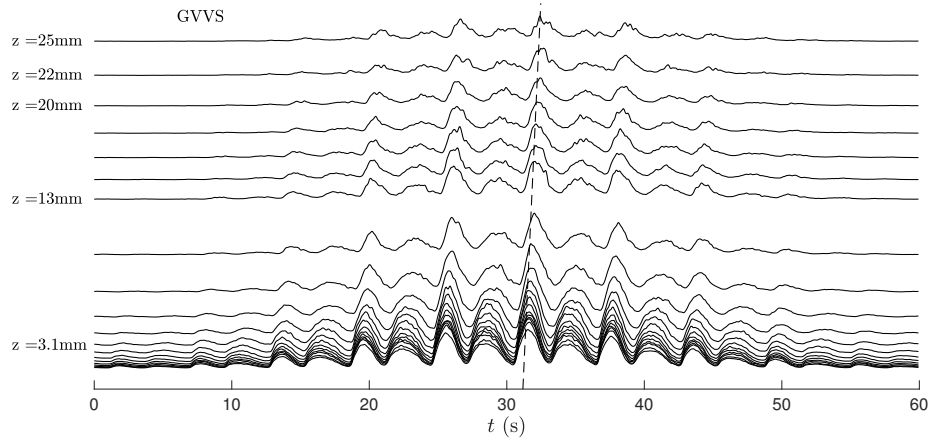


Figure 13: Upward propagation of k for GVVS: $c_k = 21$ mm/s in this case.

c_k is higher for the GV experiments, with, again, quite close agreement between c_k for GVVR (19 mm/s) and GVVS (21 mm/s). Based on the timing of peaks
 575 in u'_{rms} and w'_{rms} at different z , Sleath (1987) estimated turbulence upward propagation speed for a range of sinusoidal oscillatory flows over four different fixed beds of sediment, namely 0.2 mm sand, 1.63 mm sand, 8.12 mm gravel and 30 mm pebbles. Sleath reports an average propagation speed of c_k (mm/s) = $\omega\delta/2.27$, where Sleath's δ is boundary layer thickness measured upwards from
 580 the grain crests to the elevation where the amplitude of the defect velocity is 5% of the amplitude of u_∞ . Applying this average propagation speed to the (ω, δ) values for the highest-velocity flow case for each bed type in Sleath's Table 1, gives c_k estimates of 9, 14, 21 and 29 mm/s for the 0.2, 1.63, 8.12 and 30 mm beds respectively. These values are reasonably consistent with the ~ 14 mm/s
 585 and ~ 20 mm/s estimated for the 0.46 and 5.65 mm beds used in the present experiments.

We calculate a non-dimensional propagation speed by scaling z with δ_r and scaling the lag time by the oscillatory flow period, T , i.e. $c_k^* = c_k T / \delta_r$. The results for c_k^* are given in Table 2. They range $4.1 \leq c_k^* \leq 5.7$, with an average
 590 value of 5.0, and with no clear dependence on flow or bed roughness. The

Table 2: Upward propagation of turbulent kinetic energy

i.d.	c_k (mm/s)	a_{rms} (mm)	δ_r (mm)	c_k^* (-)	$c_{k,model}$ (mm/s)
CSSR	13	929	18.8	4.1	16
CSSS	14	926	18.5	4.5	16
CSVR	14	758	15.7	5.3	13
CSVs	14	765	15.8	5.3	14
CSVF	15	763	15.8	5.7	14
CSVB	14	766	15.8	5.3	14
CSAR	14	755	15.7	5.3	12
CSAS	13	763	15.8	4.9	14
GVVR	19	754	24.6	4.6	20
GVVS	21	778	25.2	5.0	21

corresponding value from Sleath (1987) is 2.77 ($= 2\pi/2.27$). However, this lower value (than 5.0) is mostly due to Sleath's δ being larger than δ_r . Replacing Sleath's δ with δ_r calculated using Equation 16, with values of $u_{\infty,max}$, T and a/k_s taken from Sleath's Table 1, the estimated c_k^* from Sleath's experiments
595 become 4.5, 4.2, 5.3 and 5.1 for the four bed types respectively, which are similar to the c_k^* obtained from the present experiments reported in Table 2.

Table 2 also contains c_k obtained by applying the same cross-correlation analysis to the model-predicted $k(z, t)$ for the 10 cases. The model results for c_k are in good agreement with the experimental results, echoing the good
600 agreement seen between model and experimental $\phi(z)$.

Half-cycle turbulence carry-over

Figure 14 shows example measured and predicted time-series: $k(z, t)$ at $z/\delta_r \approx 0.2$ for experiments CSSS, CSVs and CSAS. The k time-series echo the free-stream behaviour, with higher half-cycle u_∞ resulting in higher half-cycle k and the shape of $k(t)$ reflecting the shape of $u_\infty(t)$. As seen in the experiments of
605

Yuan & Dash (2017) and the model predictions of Holmedal et al. (2003), there is carry-over of k at the end of each half-cycle. For our experiments, the magnitude of the carry-over depends on the peak turbulence produced within the previous half-cycle and on the half-cycle flow shape. For the skewed flow case

610 CSVS, the carry-over from a negative flow half-cycle is greater than that from a positive flow half-cycle with similar half-cycle peak k (or half-cycle u_{pk}). This is due to the longer duration of the negative half-cycle compared with the positive half-cycle for skewed flow. For the asymmetric flow case CSAS, there is again

615 half-cycle with similar half-cycle peak k ; in this case, the greater carry-over is due to the shorter time to flow reversal following peak k in the half-cycle, resulting in less time for k to dissipate before flow reversal. The model-predicted $k(t)$ show good agreement with the experimental $k(t)$ in terms of carry-over dependence on flow shape and carry-over magnitude, although the model carry-over

620 tends to be slightly lower than the experimental results. A further observation from Figure 14 is the somewhat delayed appearance of turbulence at the start of the group, even though free-stream velocities are relatively high at these early stages. This delay is not seen in the model, which displays a more symmetric behaviour in $k(t)$ between the beginning and end of the group.

625 Analysis of the half-cycle carry-over turbulent kinetic energy, k_{co} , is presented in Figure 15, which shows k_{co} plotted against the half-cycle peak turbulent kinetic energy, k_{pk} , for $z/\delta_r \approx 0.1, 0.3$ and 0.57 for the 10 experiments (results are based on $k(t)$ smoothed using a Gaussian window with 15 data points). k_{co} increases with increasing k_{pk} as expected, but the rate of increase depends

630 on flow shape. For experiments CSSR and CSSS (Figure 15(a),(e),(i)), k_{co} is similar for positive and negative flow half-cycles with similar k_{pk} , because of the symmetry in flow shape between the positive and negative flow half-cycles. For the reasons already given, the skewed-flow experiments CSVR, CSVS, CSVF, CSVB (Figure 15(b),(f),(j)) and GVVR, GVVS (Figure 15(d),(h),(l)), and the

635 asymmetric flow experiments CSAR and CSAS (Figure 15(c),(g),(k)), all show higher k_{co} from negative half-cycles than from positive half-cycles with similar

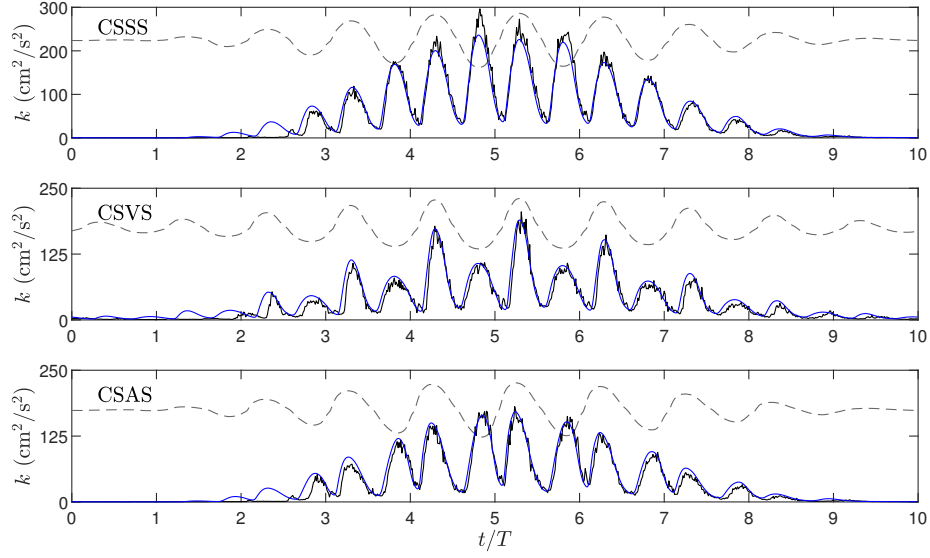


Figure 14: Measured (black) and model-predicted (blue) $k(t)$ at $z/\delta_r \approx 0.2$ for CSSS, CSVS, CSAS. Dashed-grey line: free-stream $u_\infty(t)$ (not to scale).

k_{pk} . Figure 15 also shows that, except for the few half-cycles at the start of a flow group, the k_{co} does not depend on the positioning of the flow half-cycle relative to other half-cycles, i.e. for given bed type, the carry-over is determined by k_{pk} and the half-cycle flow shape, and does not depend on when the half-cycle occurs relative to other flow half-cycles in the group. This is evidenced by the overlap of results for CSVR, CSVS, CSVF and CSVB, and indeed by the overlap of results from other corresponding regular and modulated flows.

Figure 16 shows the model results corresponding to the experimental results presented in Figure 15. The model results show good agreement with the experimental results in terms of exhibiting the effects of flow shape on the carry-over. However, the tendency seen in Figure 14 for the model to predict slightly lower carry-over than the experiments for the same k_{pk} is seen more clearly in the comparison of Figure 15 with Figure 16.

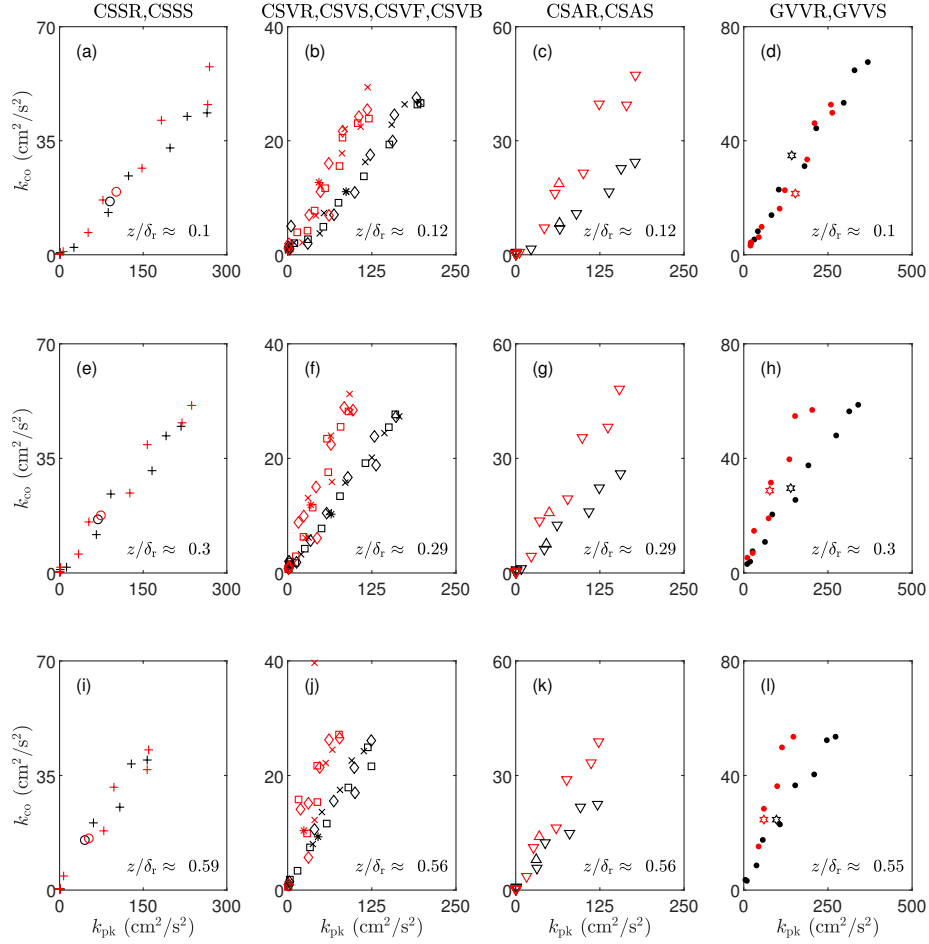


Figure 15: Experimental half-cycle carry-over turbulent kinetic energy, k_{co} , dependence on half-cycle peak turbulent kinetic energy, k_{pk} ; columns and symbols are the same as in Figure 7; results are shown for $z/\delta_\tau \approx 0.1$ (a-d), ≈ 0.3 (e-h), ≈ 0.57 (i-l); colour is used to distinguish positive (black) and negative (red) flow half-cycles.

650 *Half-cycle peak turbulence*

Figure 17 plots k_{pk} against free-stream half-cycle peak velocity, u_{pk} , for the same three elevations as Figure 15 and for all 10 cases. For these results experimental and model $k(t)$ were smoothed using a Gaussian window with 15 data points. In this figure we superimpose the experimental and model results

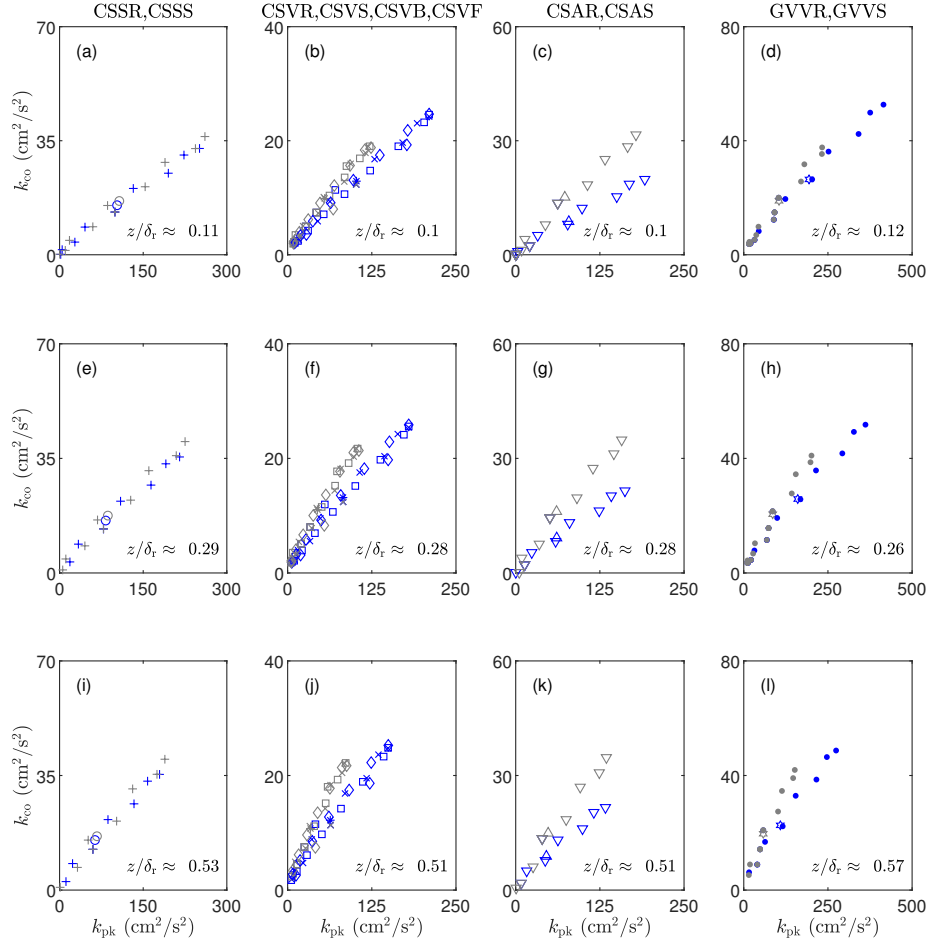


Figure 16: Model results for k_{co} corresponding to the experimental results shown in Figure 15; colour is used to distinguish positive (blue) and negative (grey) flow half-cycles.

and use the same colours as before to distinguish the experimental and model results and to distinguish positive and negative flow half-cycles. Consider first the experimental results (black and red for positive and negative flow half-cycles respectively). With the exception of a few results showing near-zero k_{pk} for relatively high velocity, (these correspond to half-cycles occurring at the beginning of the modulated flow groups), k_{pk} increases with increasing u_{pk} as expected. k_{pk} is lower for higher z/δ_r because turbulence is produced at the bed and de-

cays upwards. For the symmetric flow experiments CSSR and CSSS (Figure 17(a),(e),(i)), positive and negative half-cycles give similar k_{pk} for similar u_{pk} (black and red results overlap), again as expected. The same is true for the asymmetric-flow experiments CSAR and CSAS (Figure 17(c),(g),(k)) and for the skewed-flow experiments CSVr, CSVs, CSVf, CSVb (Figure 17(b),(f),(j)). Similar to the results presented in Figure 15, we see no dependence of k_{pk} on half-cycle position within a flow group (except for the few half-cycles at the start of a group). For CS therefore, half-cycle k_{pk} is determined by the half-cycle u_{pk} , with little influence of flow shape or flow history. This conclusion also largely applies to GVVR and GVVS (Figure 17(d),(h),(l)), except that, close to the bed ($z/\delta_r \approx 0.1$, Figure 17(d)) negative half-cycle k_{pk} is noticeably higher than positive half-cycle k_{pk} for similar u_{pk} , implying a flow shape dependency of near-bed k_{pk} for the rough-turbulent GV cases.

The model predictions in Figure 17 (blue and grey for positive and negative flow half-cycles respectively) are in general good agreement with the experiments: a quadratic dependence of k_{pk} on u_{pk} (also seen in the model results of Holmedal et al., 2003), decreasing k_{pk} with increasing z and no apparent dependence of k_{pk} on half-cycle position in the group. However, the model does not predict the higher negative half-cycle k_{pk} than positive half-cycle k_{pk} for similar u_{pk} observed close to the bed in the case of the GV experiments, i.e. the model does not show the flow shape dependency of near-bed k_{pk} seen in the GV experiments.

The combined results presented in Figures 15 to 17 show that, while there may be significant carry-over of turbulence from one half-cycle to the next half-cycle, the carry-over becomes subsumed by the developing turbulence of the new half-cycle and does not influence the peak turbulence of the new half-cycle. This result is consistent with the experimental results of Yuan & Dash (2017).

Time-averaged turbulent kinetic energy

Figure 18 presents vertical profiles of time-averaged turbulent kinetic energy, $\bar{k}(z)$, for the 10 experiments. Moving towards the bed from the free-stream, \bar{k}

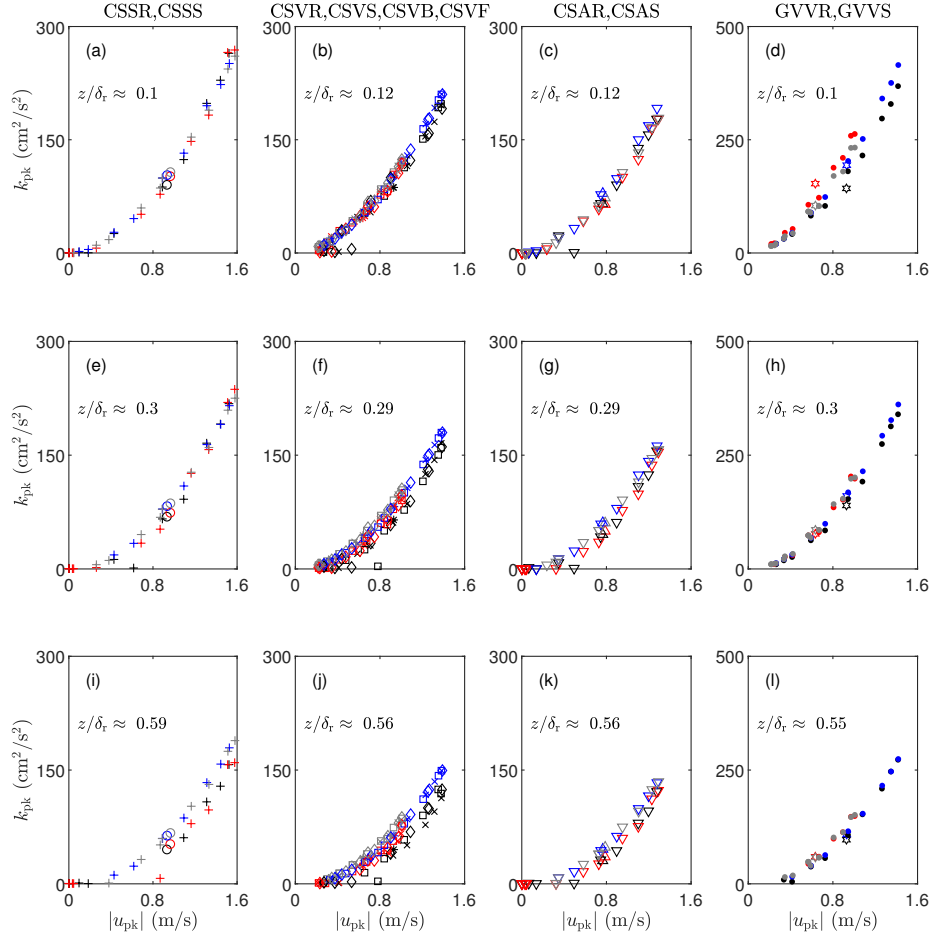


Figure 17: Experiment and model half-cycle peak turbulent kinetic energy, k_{pk} , dependence on free-stream half-cycle peak velocity, u_{pk} ; columns and symbols are the same as in Figure 7; black/red (experiment) and blue/grey (model) indicate +ve/-ve flow half-cycles.

starts to increase at $z/\delta_\tau \approx 3$. For the experimental results, \bar{k} reaches a maximum very close to the bed and decreases slightly with further proximity to the bed. \bar{k} is about a factor two greater for GV than for CS. For the CS experiments, maximum \bar{k} occurs at z/δ_τ between 0.02 and 0.03, i.e. at about one grain diameter from the bed; for GV, maximum \bar{k} occurs at $z/\delta_\tau \approx 0.12$, which is about one half a grain diameter from the bed. The experimental results show

remarkable agreement between corresponding regular and modulated flow profiles, and indeed between different flow shapes (compare Figure18(a),(b) and
 700 (c)). These results imply that \bar{k} is determined by the bed roughness and mean-square free-stream velocity, with flow shape or modulation having little or no influence. Model-predicted $\bar{k}(z)$ show good agreement with the experimental results, except in the very near-bed region where model \bar{k} monotonically increases
 as z approaches $z = z_0$. The model tends to slightly under-predict peak \bar{k} and,
 705 for CS, over-predict \bar{k} in the region $0.1 < z/\delta_r < 1$. Regular flow \bar{k} is slightly higher than modulated flow \bar{k} in the lower region of the boundary layer and is slightly higher than modulated \bar{k} at higher elevations; this feature is also seen to some extent in the experimental data.

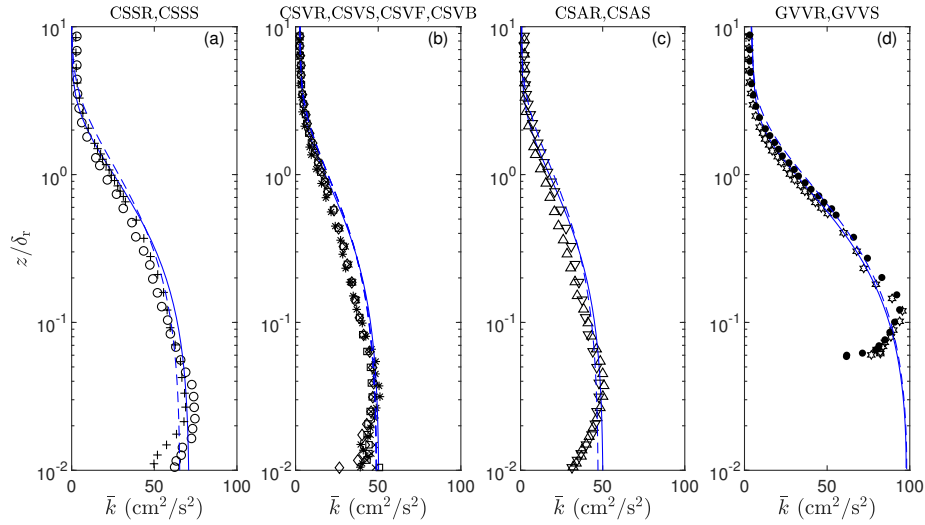


Figure 18: $\bar{k}(z)$ for the 10 cases; columns and symbols are the same as in Figure 7; model predictions for regular/modulated flows are shown by solid/dashed blue lines.

4.3. Turbulent stress and bed shear stress

710 Figure 19 shows measured and model-predicted time-series of turbulent stress, $-u'w'(t)$, at example elevation $z/\delta_r \approx 0.2$, for experiments CSSS, CSVs, CSAS and GVVS. With the exception of the first few half-cycles of the flow group when

the turbulent stress is slow to respond, the measured $-u'w'(t)$ echoes $u_\infty(t)$ in terms of general shape and magnitude. However, in the CS cases, measured
715 $-u'w'(t)$ tends to flatten at the flow reversals and is slow to increase as the flow accelerates following flow reversal, which leads to relatively narrow crests and troughs in $-u'w'(t)$ compared with $u_\infty(t)$. These effects are especially apparent in the crests of $-u'w'(t)$ for CSVS; the effects are much less apparent in the results for the rougher bed GVVS.

720 While Figure 19 shows reasonable overall agreement between measured and model-predicted $-u'w'(t)$, there are some significant differences. The flattening at flow reversal and narrowing of crests and troughs seen in the experimental results for CS are not apparent in the model CS results. In addition, half-cycle peak $-u'w'$ tends to be higher in the model than in the experiment, and
725 the model does not reproduce the sluggish response in $-u'w'$ to the initial few flow half-cycles seen in the CS (but not GV) experimental results. The differences between the experimental and model $-u'w'$ results for CS are due to the underlying assumption of rough turbulent flow in the model, whereas in reality for CS the flow is only rough turbulent under the highest-amplitude flow
730 half-cycles.

Near-bed turbulent shear stress

Figure 20 shows example time-series of experimental and model-predicted turbulent stress at (or very near) bed level for the same four experiments as in Figure 19. The model results are for $z/\delta_r = z_0/\delta_r$; the experimental results
735 are for z corresponding to the peak in the vertical profile of the time-averaged turbulent kinetic energy: $z/\delta_r \approx 0.02 - 0.03$ for CS and $z/\delta_r \approx 0.12$ for GV (Figure 18). Observations made in relation to Figure 19 apply here also: flattening of measured $(-u'w')_0(t)$ around flow reversal and narrowing of crests and troughs in the experimental CS, not seen in the model results for CS; generally
740 higher peaks in the model compared with the experiment; and sluggishness of the measured CS $(-u'w')_0(t)$ in responding to the first few flow cycles of the group, again not seen in the model CS results.

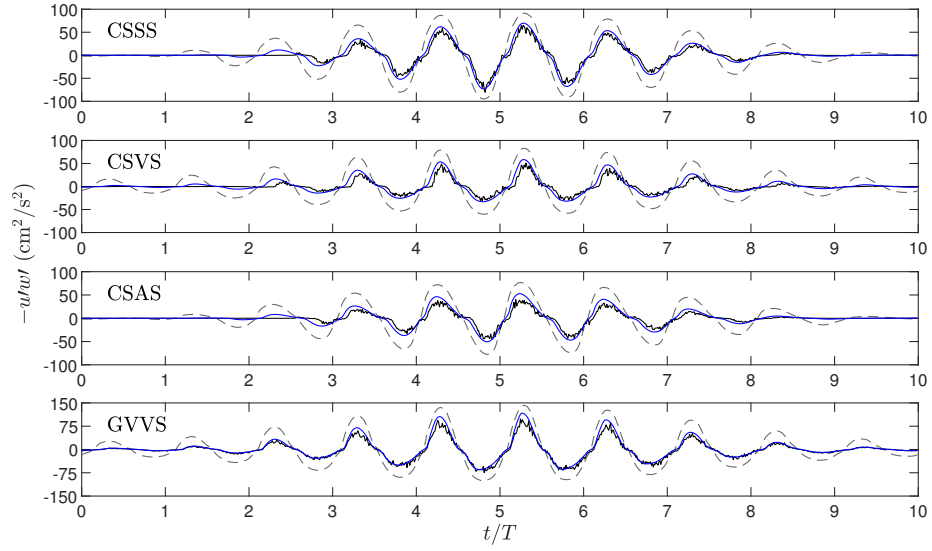


Figure 19: Measured (black) and model-predicted (blue) $-u'w'(t)$ at $z/\delta_r \approx 0.2$ for CSSS, CSVS, CSAS, GVVS. Dashed-grey line: free-stream $u_\infty(t)$ (not to scale).

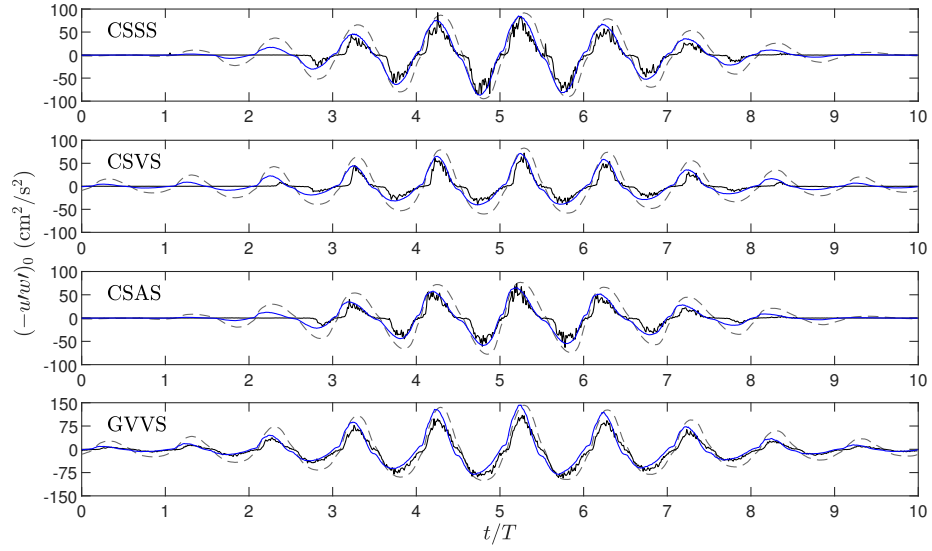


Figure 20: Measured (black) and model-predicted (blue) near-bed $-u'w'(t)$ for CSSS, CSVS, CSAS, GVVS. Dashed-grey line: free-stream $u_\infty(t)$ (not to scale).

For practical applications, the main interest generally lies in the peak shear stress. Figure 21 presents for all cases the measured and model-predicted near-bed half-cycle peak turbulent stress, $(-u'w')_{0,\text{pk}}$, plotted against the corresponding half-cycle peak free-stream velocity, u_{pk} ; separate graphs are shown for CS and GV, with colour used to distinguish positive and negative flow half-cycles as previously. For these results, measured and model-predicted $(-u'w')_{0,\text{pk}}(t)$ were smoothed using a Gaussian window with 7 data points prior to the peaks analysis. Consider first the results for CS. The experimental CS results show significant scatter at lower u_{pk} ($u_{\text{pk}} < \sim 0.7$ m/s), corresponding to the relatively low-amplitude flow half-cycles at the beginning and end of the modulated flow groups. The scatter is due to differences in turbulent stress between half-cycles of similar velocity at the two ends of the group. At higher velocities, the measured $(-u'w')_{0,\text{pk}}$ from the different experiments collapse reasonably well onto a common curve, indicating that $(-u'w')_{0,\text{pk}}$ is mainly determined by u_{pk} . There is no apparent dependence on the half-cycle position within the flow group, i.e. on flow history, and effects of flow shape are not discernible in these results. There is also good agreement between positive half-cycle and negative half-cycle $|(-u'w')_{0,\text{pk}}|$ for the same u_{pk} , again indicating little dependence on flow shape. Similarly, the model predictions for CS collapse well onto a common curve, again showing no dependence of $(-u'w')_{0,\text{pk}}$ on flow history or flow shape. The model results are consistently higher than the corresponding measured values, but the difference decreases with increasing u_{pk} (for $u_{\text{pk}} = 1.5$ m/s, model $|(-u'w')_{0,\text{pk}}|$ exceeds measured $|(-u'w')_{0,\text{pk}}|$ by approximately 10 to 15 %). The large difference at low u_{pk} , and reducing difference as u_{pk} increases, relates to the model's assumption of rough turbulent flow for all u_{pk} , while, for CS, the experimental conditions are turbulent for higher u_{pk} only.

The experimental results for GV (Figure 21(b)) follow a consistent dependence of $(-u'w')_{0,\text{pk}}$ on u_{pk} across the full range of u_{pk} , reflecting the fact that for GV, unlike for CS, significant bed shear stress is generated under the low-velocity half-cycles at the beginning and end of the flow group. There is good agreement between the stress measured under the regular flow and that

measured under the half-cycle of the modulated flow having similar u_{pk} , an
775 indication again that there is no history effect on $(-u'w')_{0,pk}$, at least for rel-
atively high-velocity flow half-cycles. In contrast to CS, the measured results
for GV show a significant difference in $(-u'w')_{0,pk}$ between positive and neg-
ative flow half-cycles, with $|(-u'w')_{0,pk}|$ being higher for negative half-cycles
than positive half-cycles with the same u_{pk} . The difference is seen across a wide
780 range of u_{pk} , increases with increasing u_{pk} (for $u_{pk} = 1$ m/s, negative half-cycle
 $|(-u'w')_{0,pk}|$ is about 60% higher than the corresponding positive half-cycle
value), and echoes the difference in half-cycle peak turbulent kinetic energy ob-
served at low z/δ_r for GV in Figure 17. The difference is not likely to be due
to the difference in flow shape between the half-cycles because we do not see
785 a corresponding difference between the positive and negative half-cycle stresses
for the velocity-skewed flows in the case of CS. We conclude that the measure-
ment of near-bed $-u'w'$ for GV is locally influenced by the bed, despite the
measurement being based on multiple x positions. The half-cycle asymmetry in
 $|(-u'w')_{0,pk}|$ is not seen in the model results, which show good agreement with
790 the measured values for negative flow half-cycles but are significantly higher
than the measured values for the positive half-cycles.

The near-bed turbulent stress estimates presented in Figure 21 are non-
dimensionalised to give the corresponding friction factors defined by $f_w =$
 $2|(u'w')_{0,pk}|/u_{pk}^2$. Figure 22 presents the experimental and model f_w plotted
795 against half-cycle a/k_s , where a is calculated for each half-cycle taking account
of flow shape (as done earlier for the results presented in Figure 8). GV and
CS results fall in the region $a/k_s < 200$ and $a/k_s > 200$ respectively. Also
shown in Figure 22 are Swart's empirical equation for f_w for turbulent condi-
tions (Swart, 1974) and Fredsøe & Deigaard's numerically-based f_w for rough
800 beds with $a/k_s > 50$ (Fredsøe & Deigaard, 1992). Note that, while the exper-
imental f_w is based on the measured near-bed turbulent shear stress, f_w from
Swart, Fredsøe & Deigaard and the present model are based on maximum total
bed shear stress, $f_w = 2|\tau_{0,max}|/(\rho u_{pk}^2)$. For oscillatory flow over a rough bed,
the total oscillatory bed shear stress is the summation of the turbulent stress

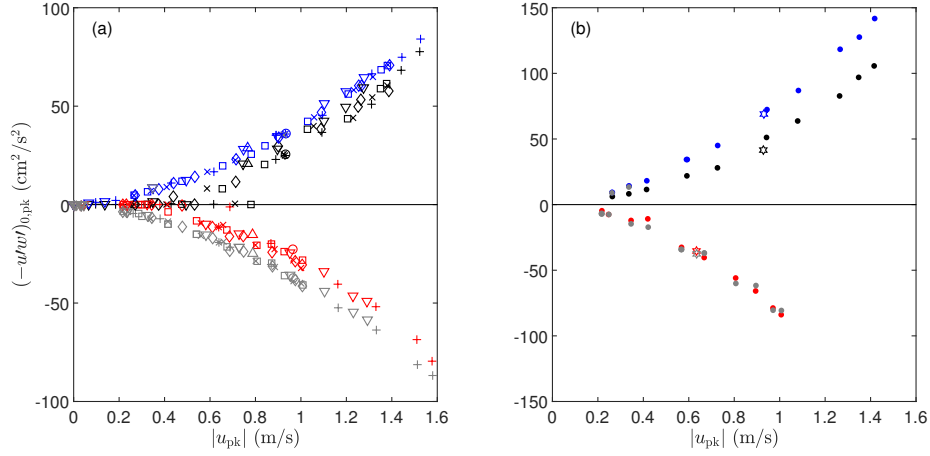


Figure 21: Experimental and model half-cycle $(-u'w')_{0,pk}$ dependence on half-cycle u_{pk} for (a) CS and (b) GV; the symbols are the same as in previous figures and colour is used to distinguish +ve/-ve flow half-cycles for the experimental (black/red) and model (blue/grey) results; note different scale for $(-u'w')_{0,pk}$ between (a) and (b).

and additional stresses due to convective transfer of momentum, correlations between vertical and horizontal periodic velocities, and form-induced pressure (Nielsen, 1992; van der A et al., 2011), and these additional stresses are more significant for GV than for CS. We expect therefore that experimental f_w based only on the near-bed turbulent stress to be less than f_w based on total bed shear stress from Swart, Fredsøe & Deigaard and the present model, especially for GV.

The experimental f_w for GV in Figure 22 are indeed lower than Swart but are generally within 25% of Fredsøe & Deigaard, the positive/negative half-cycle values being lower/higher than Fredsøe & Deigaard. The model f_w for GV agree with the experimental values for negative flow half-cycles, but are $\sim 50\%$ higher than the experimental values for the positive half-cycles, reflecting the asymmetry in $|(-u'w')_{0,pk}|$ seen in Figure 21(b). For $a/k_s > 10^3$, the CS experimental f_w follow Fredsøe & Deigaard reasonably well, but are typically 25% lower than the model predictions and 40% lower than Swart. The lower experimental f_w relative to the model and to Swart may be due to the hydraulic

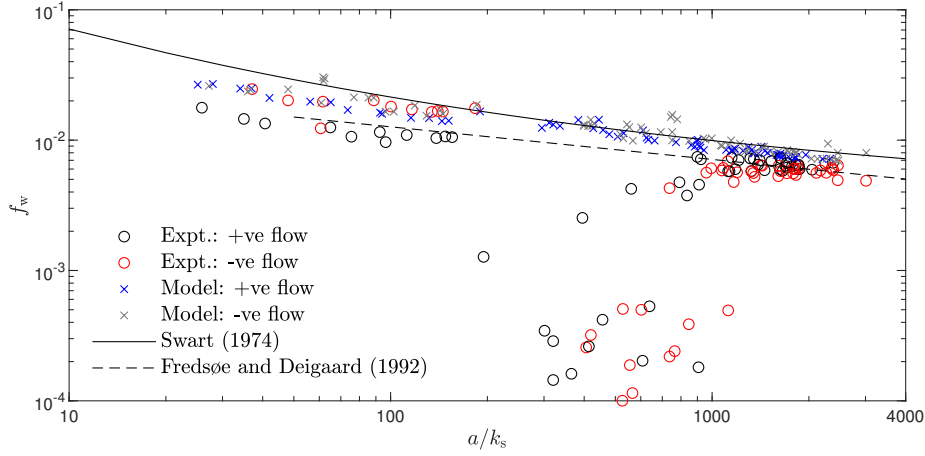


Figure 22: f_w from experiments (o, black/red for +ve/-ve flow half-cycles) and from model (x, blue/grey for +ve/-ve flow half-cycles).

regime in the experiments being more smooth- than rough-turbulent (Figure 3). The CS experimental f_w for $200 < a/k_s < 10^3$ show scatter and are lower than f_w for higher a/k_s . These f_w correspond to the low-velocity half-cycles at the start and end of the flow groups when the flow is not fully turbulent and f_w depends on Reynolds number, a/k_s and on whether the half-cycle occurs at the start or end of the flow group. Neither Swart nor Fredsøe & Deigaard are applicable to these half-cycles and the rough turbulent RANS model poorly describes their turbulence and shear stresses.

Time-averaged turbulent stress

Figure 23 shows the experimental and model-predicted vertical profiles of the time-averaged turbulent stress, $-\overline{u'w'}$, for the 10 cases. $-\overline{u'w'}$ has small magnitude, two orders of magnitude lower than the instantaneous stress (Figures 19 and 20), which makes it difficult to measure accurately. Nevertheless, the measured profiles in Figure 23 show consistent behaviour for corresponding regular and modulated flows for $z/\delta_r > 0.04$ in the case of CS (~ 2 grain diameters above the bed) and $z/\delta_r > 0.4$ in the case of GV ($\sim 3 - 4$ grain diameters above the bed), indicating the modulation has no effect on the time-averaged

stress. We note that the profiles are inconsistent with the measured $\bar{u}(z)$ presented in Figure 11 in that: $-\overline{u'w'}(z)$ is slightly negative for the symmetric flows CSSR/CSSS, when we expect it to be close to zero; $-\overline{u'w'}(z)$ is slightly negative for CSAR/CSAS, when we expect it to be slightly positive; and $-\overline{u'w'}(z)$ is marginally positive for CSVR/VS/VF/VB when we expect it to be more positive. The measured profiles are therefore slightly negatively shifted, which we expect is the result of a small error in the angular (rotational) positioning of the LDA. Below $z/\delta_r = 0.04$ and 0.4 , the measurements show scatter, partly because of the difficulty in accurately measuring $-\overline{u'w'}$ and partly because of the bed influence. The model predictions of $-\overline{u'w'}(z)$ in Figure 23 are consistent with the predicted $\bar{u}(z)$ presented in Figure 11 and, like the experimental results, show little effect of flow modulation on the time-averaged turbulent stress.

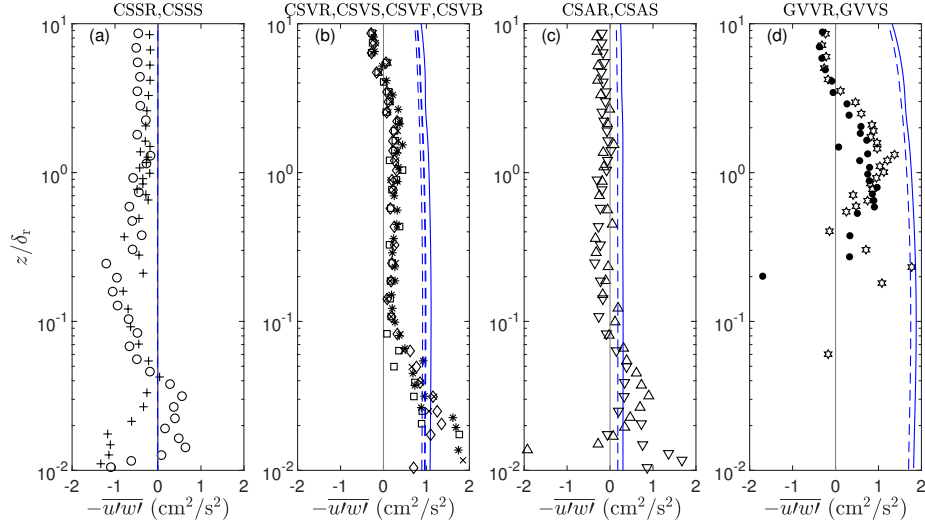


Figure 23: Experimental and model vertical profiles of $-\overline{u'w'}$; columns and symbols are the same as in Figure 7; model predictions for regular/modulated flows are shown by solid/dashed blue lines.

850 5. Conclusions

Detailed boundary layer velocity measurements have been obtained from 10 experiments involving regular and modulated oscillatory flows of various shape over two bed types: a gravel-rough bed, for which the hydraulic regime is rough turbulent, and a sand-rough bed, for which the hydraulic regime ranges from 855 transitional to close to rough turbulent as the velocity amplitude varies over the modulated flow group.

Turbulence is carried over from one flow half-cycle to the following flow half-cycle, the magnitude of which depends on the preceding half-cycle flow shape and the level of turbulence generated within that half-cycle. The carry-over can 860 be relatively large, but is quickly subsumed by the turbulence that develops as the flow accelerates during the new half-cycle, with the result that the carry-over has little or no effect on the main hydrodynamic properties of the new half-cycle. This means that boundary layer thickness, peak turbulent kinetic energy and peak turbulent stress within a half-cycle are mostly determined 865 by the magnitude and shape of the half-cycle free-stream velocity, with little or no dependence on prior conditions. These results are consistent with the observations of Yuan & Dash (2017). History effects are not completely absent however: for the sand-rough experiments, turbulence under the low-velocity half-cycles of a modulated flow is lower or higher depending on whether the 870 half-cycles precede or follow the group.

The experiments were designed such that corresponding regular and modulated flows were equivalent in terms of rms velocity, flow period, skewness and asymmetry. This has enabled the effects of flow amplitude modulation on the integrated and time-averaged hydrodynamics to be isolated and measured. The 875 results show remarkably little effect of modulation on the vertical profiles of velocity skewness, velocity asymmetry, time-averaged turbulent kinetic energy and time-averaged turbulent stress. Similarly, non-dimensional upward propagation speed of turbulent kinetic energy shows no dependence on modulation, is similar for all flows and the two bed types, and is consistent with Sleath (1987).

880 Modulation does not affect the shape of the vertical profile of time-averaged
velocity generated by non-symmetric flows, but it does reduce the magnitude,
with peak time-averaged velocity under regular flow being up to 50% higher
than that under the corresponding modulated flow.

The study includes comparison of the experimental results with predictions
885 based on a 1DV RANS model with $k - \epsilon$ turbulence closure. Overall, the model
shows reasonably good agreement with the measured time-varying and time-
averaged hydrodynamics for both the regular and modulated flows above about
one grain diameter from the bed. This includes good agreement in terms of the
intra-cycle turbulence kinetic energy, the turbulence carry-over between half-
890 cycles and the upward propagation of turbulence from the bed. For fully turbu-
lent half-cycles, predicted peak bed shear stresses tend to exceed the measured
values by about 20% on average. The model's inherent assumption of rough
turbulent flow means that turbulent kinetic energy and turbulent shear stresses
are poorly predicted for the relatively low-velocity half-cycles within modulated
895 flows over the sand-rough bed.

Data access

The phase-averaged experimental data and the output from the RANS model
will be made available via a data repository (Zenodo) if the paper is accepted
for publication by Coastal Engineering. The d.o.i. for the data will be provided
900 in the final version of the paper for publication.

Acknowledgement

The work was carried out as part of the SINBAD research project funded by
the UK's Engineering and Physical Sciences Research Council (grants EP/J00507X/1
and EP/J005541/1). MB acknowledges funding from the University of Aberdeen
905 to support his PhD. The authors acknowledge the support of the University of
Aberdeen technical staff for the experimental work, especially that of Fluids
Laboratory Technician Roy Gillanders.

References

- van der A, D. A., O'Donoghue, T., Davies, A. G., & Ribberink, J. S. (2011).
910 Experimental study of the turbulent boundary layer in acceleration-skewed
oscillatory flow. *Journal of Fluid Mechanics*, *684*, 251–283.
- van der A, D. A., Scandura, P., & O'Donoghue, T. (2018). Turbulence statistics
in smooth wall oscillatory boundary layer flow. *Journal of Fluid Mechanics*,
849, 192–230.
- 915 Abreu, T., Silva, P. A., Sancho, F., & Temperville, A. (2010). Analytical ap-
proximate wave form for asymmetric waves. *Coastal Engineering*, *57*, 656 –
667.
- Berni, C., Barthélemy, E., & Michallet, H. (2013). Surf zone cross-shore bound-
ary layer velocity asymmetry and skewness: An experimental study on a
920 mobile bed. *Journal of Geophysical Research: Oceans*, *118*, 2188–2200.
- Cavallaro, L., Scandura, P., & Foti, E. (2011). Turbulence-induced steady
streaming in an oscillating boundary layer. *Coastal Engineering*, *58*, 290–
304.
- Davies, A. (1986). A numerical model of the wave boundary layer. *Continental*
925 *Shelf Research*, *6*, 715 – 739.
- Davies, A. G., & Li, Z. (1997). Modelling sediment transport beneath regular
symmetrical and asymmetrical waves. *Continental Shelf Research*, *17*, 555–
582.
- Dixen, M., Hatipoglu, F., Sumer, B. M., & Fredsøe, J. (2008). Wave boundary
930 layer over a stone-covered bed. *Coastal Engineering*, *55*, 1–20.
- Foti, E., & Scandura, P. (2004). A low reynolds number $k-\epsilon$ model validated
for oscillatory flows over smooth and rough wall. *Coastal Engineering*, *51*,
173–184.

- Fredsøe, J., & Deigaard, R. (1992). *Mechanics of Coastal Sediment Transport*.
935 World Scientific.
- Fuhrman, D. R., Dixen, M., & Jacobsen, N. G. (2010). Physically-consistent wall boundary conditions for the $k-\omega$ turbulence model. *Journal of Hydraulic Research*, 48, 793–800.
- Henderson, S. M., Allen, J. S., & Newberger, P. A. (2004). Nearshore sandbar
940 migration predicted by an eddy-diffusive boundary layer model. *Journal of Geophysical Research*, 109, C06024, doi.
- Holmedal, L. E., Myrhaug, D., & Rue, H. (2003). The sea bed boundary layer under random waves plus current. *Continental Shelf Research*, 23, 717 – 750.
- Humbyrd, C. J. (2012). *Turbulent Combined Wave Current Boundary Layer
945 Model for Application in Coastal Waters*. Master’s thesis Massachusetts Institute of Technology, U.S.
- Jackson, P. S. (1981). On the displacement height in the logarithmic velocity profile. *Journal of Fluid Mechanics*, 111, 15–25.
- Jensen, B. L., Sumer, B., & Fredsøe, J. (1989). Turbulent oscillatory boundary
950 layers at high Reynolds numbers. *Journal of Fluid Mechanics*, 206, 265–297.
- Jonsson, I. G. (1963). Measurements in the turbulent wave boundary layer. In *Proc. 10th Congress IAHR, London* (pp. 85–92).
- Jonsson, I. G., & Carlsen, N. A. (1976). Experimental and theoretical investigations in an oscillatory turbulent boundary layer. *Journal of Hydraulic
955 Research*, 14, 45–60.
- Justesen, P. (1991). A note on turbulence calculations in the wave boundary layer. *Journal of Hydraulic Research*, 29, 699–711.
- Malarkey, J., & Davies, A. G. (2012). Free-stream velocity descriptions under waves with skewness and asymmetry. *Coastal Engineering*, 68, 78–95.

- 960 Nielsen, P. (1992). *Coastal bottom boundary layers and sediment transport*.
World Scientific.
- Ranasoma, K., & Sleath, J. (1992). Velocity measurements close to rippled beds.
In *Proc. 23rd Int. Conf. on Coastal Eng., Venice* (pp. 2383–2396). Venice,
Italy: Am. Soc. of Civ. Eng.
- 965 Rodi, W. (1993). *Turbulence models and Their Application in Hydraulics - A
State of the Art Review*. Brookfield, Vt: A. A. Balkema.
- Sana, A., Ghumman, A.-R., & Tanaka, H. (2009). Modeling of a rough-wall
oscillatory boundary layer using two-equation turbulence models. *Journal of
Hydraulic Engineering*, 135, 60–65.
- 970 Sana, A., & Tanaka, H. (2000). Review of $k - \epsilon$ model to analyze oscillatory
boundary layers. *Journal of Hydraulic Engineering*, 126, 701–710.
- Sleath, J. F. A. (1987). Turbulent oscillatory flow over rough beds. *Journal of
Fluid Mechanics*, 182, 369–409.
- Soulsby, R. (1983). The bottom boundary layer of shelf seas. In B. Johns
975 (Ed.), *Physical oceanography of coastal and shelf seas* (pp. 189–266). Elsevier,
Amsterdam.
- Svendsen, I. A. (1987). Analysis of surf zone turbulence. *Journal of Geophysical
Research-Oceans*, 92, 5115–5124.
- Swart, D. H. (1974). Offshore sediment transport and equilibrium beach profiles.
980 In *Publication No. 131*. Delft Hydraulics Laboratory.
- Yuan, J., & Dash, S. M. (2017). Experimental investigation of turbulent wave
boundary layers under irregular coastal waves. *Coastal Engineering*, 128, 22
– 36.
- Yuan, J., & Madsen, O. S. (2014). Experimental study of turbulent oscillatory
985 boundary layers in an oscillating water tunnel. *Coastal Engineering*, 89, 63–
84.